Nonlinear Dynamics of Three-Dimensional Solitary Waves

by

Yeunwoo Cho

B.S., School of Electrical Engineering, Seoul National University, Korea, 2001
S.M., Mechanical Engineering, Massachusetts Institute of Technology, 2004

Submitted to the Department of Mechanical Engnieering
in partial fulfillment of the requirements for the degree of

Doctor of Philosophy in Mechanical Engineering

at the

MASSACHUSETTS INSTITUTE OF TECHNOLOGY

June 2010

Author .....
Department of Mechanical Engnieering
May 18, 2010

Certified by .....
Triantaphyllos R. Akylas
Professor
Thesis Supervisor

Accepted by .....
David E. Hardt
Chairman, Committee on Graduate Students

Nonlinear Dynamics of Three-Dimensional Solitary Waves

by

Yeunwoo Cho

Submitted to the Department of Mechanical Engnieering
on May 18, 2010, in partial fulfillment of the
requirements for the degree of
Doctor of Philosophy in Mechanical Engineering

Abstract

In problems of dispersive wave propagation governed by two distinct restoring-force mechanisms, the phase speed of linear sinusoidal wavetrains may feature a minimum, $c_{\min}$, at non-zero wavenumber, $k_{\min}$. Examples include waves on the surface of a liquid in the presence of both gravity and surface tension, flexural waves on a floating ice sheet, in which case capillarity is replaced by the flexural rigidity of the ice, and internal gravity waves in layered flows in the presence of interfacial tension. The focus here is on deep-water gravity–capillary waves, where $c_{\min} = 23$ cm/s with corresponding wavelength $\lambda_{\min} = 2\pi/k_{\min} = 1.71$ cm. In this instance, ignoring viscous dissipation, $c_{\min}$ is known to be the bifurcation point of two-dimensional (plane) and three-dimensional (fully localized) solitary waves, often referred to as "lumps"; these are nonlinear disturbances that propagate at speeds below $c_{\min}$ without change of shape owing to a perfect balance between the opposing effects of wave dispersion and nonlinear steepening. Moreover, $c_{\min}$ is a critical forcing speed, as the linear inviscid response to external forcing moving at $c_{\min}$ grows unbounded in time, and nonlinear effects as well as viscous dissipation are expected to play important parts near this resonance.

In the present thesis, various aspects of the dynamics of gravity–capillary lumps are investigated theoretically. Specifically, it is shown that steep gravity–capillary lumps of depression can propagate stably and they are prominent nonlinear features of the forced response near resonant conditions, in agreement with companion experiment for the generation of gravity–capillary lumps on deep water. These findings are relevant to the generation of ripples by wind and to the wave drag associated with the motion of small bodies on a free surface.

Thesis Supervisor: Triantaphyllos R. Akylas
Title: Professor

Acknowledgments

First and foremost, I thank my advisor and the committee chair, Professor Triantaphyllos R. Akylas for his contribution to this thesis work. His scholarly and sincere guidance has led me on the right path while doing my PhD work at MIT. I was really lucky to have him as my advisor during my PhD work. What I learned from him will play an important part in my future career. This work was sponsored by NSF and AFOSR. I thank the other committee members, Professor Rodolfo R. Rosales and Professor Thomas Peacock for their constructive suggestions and feedbacks about this thesis work. I thank Dr. Tian Tian, who was my advisor while doing my SM work at MIT. I learned how to do simulation and how to think as an engineer. I thank Professor Gilbert Strang for giving me the opportunity to work as a TA in his courses, Mathematical Methods for Engineers I & II. I learned how to solve mathematical problems in a new and efficient way. I thank Leslie Regan for her cheerful support from admission to MIT to graduation from MIT. I specially thank Benjamin Druecke in the lab. As a friend, he made my life enjoyable during the PhD work. He also helped me finish this thesis by sincere proofreading. I was lucky to have him as a friend and a colleague during the life at MIT. I thank Youssef Mroueh and Themistocles Resvanis in the neighbor lab for their friendships. I thank many Korean friends at MIT. Specially, I thank Dr. Jongmin Shim and Dr. Heejin Lee for their cheerful support and friendships from the same time when we started graduate studies at MIT until they graduated from MIT. I thank Dr. James Diorio and Professor James Duncan at University of Maryland for their companion experimental work related to Chapter 4 in this thesis. I thank many friends in Korea. Specially, I thank Sukhee Han for his cheer and freindship. I heartily thank Youngcheon Park for her evergreen support. Last but not least, I thank my parents and my little brother for their endless support. Specially, I thank my late father who passed away last year. He always wanted to see me graduate from MIT. I wish both my father and my mother together could see me finishing my PhD work. Without them, I could not carry on and finish my PhD studies at MIT.

Contents

List of Figures

List of Tables

Chapter 1

Introduction

1.1 Gravity solitary waves

When dispersion and nonlinearity are exactly balanced in a dispersive wave system, locally confined steady waves of permanent form, or solitary waves, may arise. John Scott Russell, a Scottish engineer made the first observation of a solitary wave at the Union Canal in Edinburgh in 1834. He described his observation as "the form of a large solitary elevation, a rounded, smooth and well-defined heap of water, which I have called the Wave of Translation" (Russell 1844). Dispersive waves such as water waves can be modeled by nonlinear partial differential equations. The relevant equation for Russell's solitary wave is the Korteweg–de Vries (KdV) equation, which describes the dynamics of long waves on the surface of shallow water and admits a 'sech^2' two-dimensional (2-D) solitary wave solution (Korteweg & de Vries 1895). The KdV equation is a generic equation in that it can describe weakly nonlinear long-wave phenomena in various other fields such as plasma physics, optics, astrophysics and biomechanics. The KdV solitary wave is a nonlinear gravity solitary wave of elevation. In the absence of surface tension, the phase speed of linear gravity waves features a maximum at zero wavenumber (long wave). The KdV soliary wave of elevation exists when its speed is above the linear phase-speed maximum.

1.2 Gravity–capillary solitary waves

In contrast to pure gravity waves, the linear phase speed features a minimum if both gravity and surface tension are equally important. The resuling waves are gravity–capillary solitary waves. Depending on the wavenumber where the phase-speed minimum occurs, there are two types of solitary waves. When the phase-speed minimum occurs at zero wavenumber (long wave), two-dimensioanl (2-D) KdV solitary waves of depression and three-dimensional (3-D) Kadomtsev-Petviashvili (KP-I) solitary waves of depression (Kadomtsev & Petviashvili 1970) exist when their speeds are below the linear phase-speed minimum. On the other hand, when the phase-speed minimum occurs at non-zero wavenumber, there exist different types of 2-D and 3-D gravity–capillary solitary waves having speeds below the linear phase-speed minimum. In contrast to well established KdV or KP-I solitary waves, the latter type of 2-D gravity–capillary solitary waves and 3-D gravity–capillary solitary waves (commonly refered to as 'lumps') were discovered only recently (Akylas 1993; Longuet-Higgins 1993; Kim & Akylas 2005; Parau, Vanden-Broeck & Cooker 2005) and are the subject of the present thesis work.

Previous work mostly dealt with the existence (Groves & Sun 2005) and steady profiles of these gravity–capillary depression solitary waves with propagation speeds less than the linear phase-speed minimum (Longuet-Higgins 1989; Vanden-Broeck & Dias 1992; Parau, Vanden-Broeck & Cooker 2007). At low speeds below $c_{\min}$, they are fully localized disturbances with steep depression. At speeds close to $c_{\min}$, they are wavepacket-type disturbances with small amplitudes. The stability and the related dynamics of these gravity–capillary wavse were studied only recently. 2-D gravity–capillary solitary depression waves are stable to longitudinal perturbations (Calvo & Akylas 2002). However, when subject to transverse perturbations, they are unstable and eventually transform into steep 3-D gravity–capillary solitary depression waves (Kim & Akylas 2006). Compared to their 2-D counterparts, 3-D gravity–capillary solitary depression waves have different stability characteristcs. While 3-D steep gravity–capillary solitary depression waves are stable to longitudinal perturbations,

small-amplitude 3-D gravity–capillary solitary depression waves of wavepacket type are unstable to longitudinal pertubations (Akylas & Cho 2008; Chapter 2). These gravity–capillary waves have also been observed in experiments. Zhang (1995) reported evidence of 3-D gravity–capillary solitary depression waves on the surface of deep water in a wind-wave experiment. Later, Longuet-Higgins & Zhang (1997) tried to generate 2-D gravity–capillary solitary depression waves on the surface of deep water in the laboratory. They used a 2-D slit through which compressed air was blown onto the surface of stream of deep water. They reported persistent lateral instability in the 2-D plane solitary waves. Based on these studies, only steep 3-D gravity–capillary solitary depression waves are expected to be physically relevant and, therefore, are the main focus of the present thesis work.

1.3 Objective of thesis work

The main purpose of the present thesis work is to reveal the physics governing the dynamic behavior of 3-D gravity–capillary depression solitary waves generated by a moving pressure forcing on the surface of deep water. Motivated by aformentioned studies, combined experimental and theoretical studies on 3-D gravity–capillary solitary depression waves were proposed by research groups from University of Maryland (Professor James Duncan and Dr. James Diorio) and MIT (Professor Triantaphyllos R. Akylas and author). Particularly, the main focus of this joint work is on the generation of 3-D gravity–capillary depression solitary waves on deep water. In the experiment, three different behavioral states (state I, II, and III) are identified according to forcing speeds. When the forcing speed is low, a simple 3-D depression was observed just below the moving forcing. This is essentially the linear response, and this state is refered to as state I. As the forcing speed is increased towards $c_{\min}$, they observed steep steady 3-D gravity-capillary solitary depression waves following just behind the moving forcing, and this state is referred to as state II. In addition, in state II, the response of maximum depression is independent of the forcing strength. Finally, near the resonance when forcing speed is close to $c_{\min}$, they observed that 3-D

gravity–capillary solitary depression waves are shed outward in the oblique directions in a time-periodic manner and decay due to viscous dissipation. This state is referred to as state III. Overall, 3-D gravity–capillary solitary depression waves observed in the experiment are steep and, therefore, nonlinearity is not weak. In addition, they are in the gravity–capillary range, so viscous dissipation cannot be neglected. Finally, the interplay between nonlinearity and viscous dissipation is very delicate, which is implied in the characteristics of state II and state III.

Related to the main objective of explaining the experimental results, several preliminary theoretical studies were done in advance and, also, in parallel with the companion experiment. The first work is to investigate the stability of 3-D gravity–capillary solitary depression wave according to its steepness or propagation speed (Chapter 2). The contents of chapter 2 are based on the paper by Akylas & Cho (2008). A linear stability analysis is carried out to reveal the stabilty of 3-D gravity–capillary solitary depression waves according to the wave steepness. Also, the related nonlinear dynamics is investigated numerically. This chapter provides the stabilty criteria which is related to the existence of stable steep 3-D gravity–capillary solitary depression waves observed in the companion experiment.

The second work is to investigate the dynamics of 2-D gravity–capillary solitary depression waves generated by a 2-D moving pressure forcing (Chapter 3). The contents of chapter 3 are based on the paper by Cho & Akylas (2008). This chapter is a preliminary study leading into the investigation of forced 3-D gravity–capillary solitary depression waves with viscous dissipation. Compared to the free gravity–capillary solitary waves without forcing and viscous dissipation, little is known about the forced gravity–capillary waves with viscous dissipation, even in the 2-D solitary wave case. The purpose here is to study both steady and unsteady responses according to forcing speeds under the effects of unsteadiness, nonlinearity and viscous dissipation. Particular attention is paid to the resonant condition where forcing speed is close to $c_{\min}$. This preliminary work regarding forced 2-D solitary waves is expected to provide a partial explanation for the three different behavioral states observed in the experiments and, also reveal the combined effects of nonlinearity and viscous

dissipation when forcing speed is close to $c_{\min}$.

Chapter 4 is the capstone of this research and provides a model explaining the experimental behavior of steep 3-D forced gravity–capillary solitary depression waves with viscous dissipation. The contents of chapter 4 are based on the paper by Diorio, Cho, Duncan & Akylas (2009) and further results in preparation for the publication of papers (Experimental part: Diorio, Cho, Duncan & Akylas, Theoretical & Computational part: Cho, Diorio, Akylas & Duncan). This chapter is directly related to the companion experimental results. The purpose is to study both steady and unsteady responses according to forcing speeds under the effects of three-dimensionality, unsteadiness, nonlinearity and viscous dissipation. Particular attention is paid to the resonant condition where forcing speed is close to $c_{\min}$. This work provides full, although qualitative, explanation for the three different behavioral states observed in the experiment and the combined effects of nonlinearity and viscous dissipation when forcing speed is close to $c_{\min}$.

Chapter 2

On the stability of lumps and wave collapse in water waves

2.1 Introduction

Unlike their plane-wave counterparts, 3-D solitary waves localized in all directions, commonly referred to as lumps, arise in dispersive wave systems under rather special conditions. On physical grounds, for a lump to remain locally confined, its speed must be such that no linear wave can co-propagate with the main wave core. This is feasible when the linear phase speed features a minimum so lumps propagate below this minimum.

In the classical water-wave problem, in particular, the phase speed features a minimum only if both gravity and surface tension are important, and two distinct types of lumps arise: firstly, in the high-surface-tension regime (Bond number, $B > \frac{1}{3}$), where the phase-speed minimum occurs at zero wavenumber, lumps bifurcate at the linear-long-wave speed and are generalizations of the depression solitary waves of the Korteweg–de Vries (KdV) equation in shallow water. Secondly, for $B < \frac{1}{3}$, on water of finite or infinite depth, where the phase-speed minimum is realized at a non-zero wavenumber, lumps bifurcate from linear sinusoidal waves of finite wavelength at this minimum and, in the near-linear limit, behave like localized wavepackets with envelope and crests moving at the same speed.

Although shallow-water lumps have been studied extensively, lumps of the wavepacket type were discovered only recently. Using an asymptotic approach, Kim & Akylas (2005) constructed small-amplitude wavepacket lumps slightly below the minimum gravity–capillary phase speed. In this limit, lumps can be approximated in terms of a particular steady solution (ground state) of an elliptic equation system that governs the coupled evolution of the envelope along with the induced mean flow. We shall refer to this system as the Benney–Roskes–Davey–Stewartson (BRDS) equations, as the coupling of the envelope to the mean flow for a gravity wavepacket with two-dimensional modulations was first studied by Benney & Roskes (1969), followed by Davey & Stewartson (1974); the effects of surface tension were included later (Djordjevic & Redekopp 1977). The asymptotic analysis of Kim & Akylas (2005) suggests that two branches of symmetric lumps, one of elevation and the other of depression, bifurcate at the minimum phase speed; they are fully localized counterparts of the two symmetric plane-solitary-wave solutions that bifurcate there as well (see, for example, Dias & Kharif 1999).

In an independent numerical study, Parau, Vanden-Broeck & Cooker (2005) computed symmetric elevation and depression gravity–capillary lumps on deep water with speed less than the minimum phase speed. In the small-amplitude limit, consistent with the asymptotic analysis, these lumps behave like wavepackets and, as the steepness increases, they transform into fully localized disturbances whose centreline profiles resemble steep plane solitary waves on deep water computed in earlier studies (Longuet-Higgins 1989; Vanden-Broeck & Dias 1992). More recently, the same authors also presented computations of similar gravity–capillary lumps on water of finite depth (Parau, Vanden-Broeck & Cooker 2007). Finally, a rigorous existence proof of gravity–capillary lumps was given in Groves & Sun (2005).

The studies cited above deal exclusively with steady wave profiles, and little is known about the stability properties and dynamics of lumps that bifurcate at the minimum gravity–capillary phase speed for $B < \frac{1}{3}$. In an attempt to fill this gap, Kim & Akylas (2007) examined the stability of plane solitary waves of depression to long-wavelength transverse perturbations. While stable to longitudinal perturbations

(Calvo & Akylas 2002), depression solitary waves turn out to be transversely unstable, suggesting a possible generation mechanism of lumps, similar to that of shallow-water lumps which arise from the transverse instability of KdV solitary waves of depression. This scenario was confirmed in Kim & Akylas (2006) using a model equation for weakly nonlinear long interfacial waves in a two-layer configuration. In this instance, according to unsteady numerical simulations, transverse instability leads to the formation of lumps, that propagate stably at a different speed, thus separating from the rest of the disturbance.

However, there is also reason to suspect that, close to their bifurcation point at least, gravity–capillary lumps of the wavepacket type are unstable, since, in the small-amplitude limit, they are related to the ground state of the BRDS equations. This equation system predicts the formation of a singularity at a finite time, known as wave collapse, owing to nonlinear focusing when the initial condition exceeds a certain threshold (Ablowitz & Segur 1979; Papanicolaou *et al.* 1994). Given that the ground state is on the borderline between existence for all time and collapse, one would expect small-amplitude lumps to be prone to nonlinear focusing; the numerical simulations of Kim & Akylas (2006) though did not reveal any sign of a related instability.

As a first step towards a comprehensive study of the stability properties of gravity–capillary lumps of the wavepacket type, rather than tackling the full water-wave equations, we shall discuss a simpler model problem. Specifically, we consider the fifth-order KP equation, an extension to two spatial dimensions of the fifth-order KdV equation, that describes weakly nonlinear long water waves for Bond number close to $\frac{1}{3}$. While ignoring viscous effects cannot be justified under these flow conditions, the fifth-order KP equation admits lumps of the wavepacket type analogous to those found in the full water-wave problem for $B < \frac{1}{3}$, and provides a useful model for theoretical purposes.

A linear stability analysis of depression lumps (the primary solution branch) of the fifth-order KP equation confirms that they are unstable in the small-amplitude limit. An exchange of stability takes place at a finite wave steepness though, above

which lumps become stable. Moreover, based on unsteady numerical simulations, a small-amplitude wavepacket, under conditions for which it would have experienced wave collapse according to the BRDS equations, in fact evolves to an oscillatory state near a finite-amplitude lump that is stable. This clarifies the meaning of the wave collapse predicted by the approximate envelope equations and suggests an explanation for the emergence of stably propagating finite-amplitude lumps in the simulations of Kim & Akylas (2006).

Even though the present chapter deals with a model equation only, it is likely that locally confined gravity–capillary wavepackets in the full water-wave problem also would have a tendency to form steep lumps as a result of nonlinear focusing. This would seem consistent with laboratory observations of wind-driven gravity–capillary waves having profiles similar to those of steep depression lumps (Zhang 1995).

2.2 Preliminaries

As remarked earlier, in order for lumps to be possible in the water-wave problem, it is necessary that the linear phase speed features a minimum, and this requires both gravity and surface tension to be present. Using the water depth h as lengthscale and $(h/g)^{1/2}$ as timescale, g being the gravitational acceleration, the character of gravity–capillary lumps hinges on the value of the Bond number $B = \sigma/(\rho g h^2)$, where σ denotes the surface tension and ρ the fluid density. This is clear from the dispersion relation, $\omega^2 = k(1 + Bk^2)\tanh k$, k being the wavenumber and ω the wave frequency, according to which the minimum of the phase speed ω/k is realized at $k = 0$ when $B > \frac{1}{3}$, whereas for $B < \frac{1}{3}$, it occurs at a non-zero wavenumber, $k = k_m$. Accordingly, in the former case, lumps are two-dimensional generalizations of KdV solitary waves of depression that also bifurcate at $k = 0$, while, in the latter case, lumps are fully localized counterparts of the plane solitary wavepackets that bifurcate at $k = k_m$ as well.

As our interest centres on lumps of the wavepacket type, we shall take $B < \frac{1}{3}$, and, for convenience, it will be further assumed that B is close to $\frac{1}{3}$ so that $k_m \ll 1$. The

neighborhood of the phase-speed minimum may then be captured via a long-wave approximation ($k \ll 1$) to the dispersion relation:

$$\omega = k\left\{1 + \tfrac{1}{2}(B - \tfrac{1}{3})k^2 + \tfrac{1}{90}k^4 + \cdots\right\}. \tag{2.1}$$

Combined with a quadratic nonlinear term of the KdV type, (2.1) leads to the fifth-order KdV equation, that has served as the starting point in several prior theoretical investigations of plane solitary waves of the wavepacket type (see Grimshaw 2007 for a review). In the same vein, we shall make use of the fifth-order KP equation, an extension to two spatial dimensions of the fifth-order KdV equation, in order to discuss lumps of the wavepacket type. To this end, assuming nearly uni-directional wave propagation along x, the leading-order effects of transverse (y-) variations are taken into account in (2.1) by writing $k = (l^2 + m^2)^{1/2} \approx l + \frac{1}{2}m^2/l$, l being the longitudinal and $m \ll l$ the transverse wavenumber components.

The fifth-order KP equation then follows from this weakly two-dimensional approximation to the linear dispersion relation, combined with a KdV-type quadratic nonlinear term. A systematic derivation was presented in Paumond (2005). Here, we shall work with the fifth-order KP equation (for $B < \frac{1}{3}$) in the normalized form

$$\left\{\eta_t + 3(\eta^2)_x + 2\eta_{xxx} + \eta_{xxxxx}\right\}_x + \eta_{yy} = 0, \tag{2.2}$$

where $\eta(x, y, t)$ stands for a variable associated with the wave distrubance, such as the free-surface elevation, in a frame moving with the linear-long-wave speed. The linear dispersion relation of the model equation (2.2) for uni-directional propagation along x,

$$\omega = -2k^3 + k^5, \tag{2.3}$$

is of the same form as (2.1) when allowance is made for the change in reference frame.

In preparation for discussing the dynamics of lumps, we first consider small-amplitude modulated wavepackets of (2.2) and obtain the corresponding evolution equations. This derivation follows along the lines of the classical weakly nonlinear sta-

bility theory (Stuart 1960). Briefly, introducing the amplitude parameter $0 < \epsilon \ll 1$, the appropriate expansion takes the form

$$\eta = \tfrac{1}{2}\epsilon\left\{S(X,Y,T)\mathrm{e}^{\mathrm{i}\theta} + \text{c.c.}\right\} + \epsilon^2 S_0(X,Y,T) + \epsilon^2\left\{S_2(X,Y,T)\mathrm{e}^{2\mathrm{i}\theta} + \text{c.c.}\right\} + \cdots, \quad (2.4)$$

where $\theta = kx - \omega t$, k and ω being the carrier wavenumber and frequency, respectively, which satisfy the dispersion relation (2.3), and $(X,Y,T) = \epsilon(x,y,t)$ are the 'slow' envelope variables.

Upon substituting (2.4) into (2.2) and collecting zeroth-harmonic terms, the induced mean flow S_0 satisfies, to leading order:

$$S_{0XT} + S_{0YY} = -\tfrac{3}{2}(|S|^2)_{XX}. \quad (2.5)$$

Similarly, collecting second-harmonic and primary-harmonic terms, the envelope $S(X,Y,T)$ of the primary harmonic satisfies

$$\mathrm{i}(S_T + c_g S_X) + \epsilon(\tfrac{1}{2}c_g' S_{XX} + \tfrac{1}{k}S_{YY}) + \tfrac{3}{2}\epsilon\frac{S^2S^*}{k(5k^2-2)} - 6\epsilon k S S_0 = 0, \quad (2.6)$$

where $c_g = \mathrm{d}\omega/\mathrm{d}k$, $c_g' = \mathrm{d}^2\omega/\mathrm{d}k^2$ and $*$ denotes complex conjugate.

As expected, to leading order, the wavepacket propagates with the group velocity c_g. Adopting a reference frame moving with c_g, $X' = X - c_g T$, and defining $T' = \epsilon T$, it follows from (2.5) and (2.6) (after dropping the primes) that S and S_0 satisfy

$$-c_g S_{0XX} + S_{0YY} = -\tfrac{3}{2}(|S|^2)_{XX}, \quad (2.7a)$$

$$\mathrm{i}S_T + \tfrac{1}{2}c_g' S_{XX} + \frac{1}{k}S_{YY} + \tfrac{3}{2}\frac{S^2S^*}{k(5k^2-2)} - 6kSS_0 = 0. \quad (2.7b)$$

The coupled-equation system (2.7a) and (2.7b) is of the same form as the BRDS equations that govern the evolution of the wave envelope and the induced mean flow of a modulated wavepacket in the water-wave problem.

As explained by Ablowitz & Segur (1979), the signs of the various coefficients in these equations are critical in determining the character of the solution. Here, of

particular interest is the case of both (2.7a) and (2.7b) being elliptic; this requires $c_g < 0$ and $c_g' > 0$, which is realized if $\sqrt{3/5} < k < \sqrt{6/5}$. For k in this range, moreover, the coefficient of the cubic term in (2.7b) is positive, implying that the self-interaction of the envelope has a focusing effect, and the sign of the second nonlinear term in (2.7b) is such that the interaction of the envelope with the mean flow enhances this nonlinear self-focusing. As a result, when $\sqrt{3/5} < k < \sqrt{6/5}$, the BRDS equations (2.7a) and (2.7b), predict the formation of a singularity in finite time, or so-called wave collapse, of localized initial conditions above a certain threshold amplitude (Ablowitz & Segur 1979; Papanicolaou *et al.* 1994). In the water-wave problem, this situation arises for gravity–capillary wavepackets in sufficiently deep water, suggesting that a small-amplitude wave pulse under these flow conditions would evolve to a peaked nonlinear disturbance.

It is well known (see, for example, Papanicolaou *et al.* 1994; Ablowitz, Bakirtas & Ilan 2005) that the threshold for wave collapse is provided by a special locally confined solution of (2.7a) and (2.7b), so-called ground state, $S = \bar{S}(X, Y)\exp(\mathrm{i}T)$. Physically, this solution, when combined with the carrier signal, corresponds to a fully localized wavepacket with envelope of permanent form moving with the group speed c_g and crests travelling at the linear phase speed, ω/k, slightly modified by nonlinear effects. In general, as these two speeds are different, the disturbance, as a whole, does not represent a lump. However, at the specific wavenumber $k = k_m = 1$ and frequency $\omega = \omega_m = -1$ corresponding to the minimum of the linear phase speed, the group speed $c_g|_m$ is equal to $\omega_m/k_m = -1$ so the minimum phase speed becomes the bifurcation point of lumps of the wavepacket type. It is important to note that $k_m = 1$ is within the range $\sqrt{3/5} < k < \sqrt{6/5}$ where the BRDS equations (2.7a) and (2.7b) are of the elliptic–elliptic focusing type.

Returning to (2.4), near their bifurcation point, these lumps can be approximated as localized wavepackets with envelope and crests moving at the same speed: $\bar{\eta} = \epsilon\bar{S}(\xi, Y)\cos(x - ct) + \cdots$, where $\xi = \epsilon(x - ct), c = -1 - \epsilon^2$, $\bar{S}$ being the ground-state solution of the BRDS equations for $k = k_m = -1$; from (2.7a) and (2.7b), it follows

that $\bar{S}$ satisfies the coupled system

$$\bar{S}_{0\xi\xi} + \bar{S}_{0YY} = -\tfrac{3}{2}(|\bar{S}|^2)_{\xi\xi}, \tag{2.8a}$$

$$-\bar{S} + 4\bar{S}_{\xi\xi} + \bar{S}_{YY} + \tfrac{1}{2}\bar{S}^3 - 6\bar{S}_0\bar{S} = 0. \tag{2.8b}$$

Note that two symmetric solution branches bifurcate at $\epsilon = 0$, one corresponding to elevation and the other to depression lumps, depending on whether the maximum of $\bar{S}$ at the origin $\xi = Y = 0$ coincides with a crest or a trough, respectively. Small-amplitude lumps near the minimum phase speed of the full gravity–capillary problem for $B < \frac{1}{3}$ were constructed in a similar way by Kim & Akylas (2005). In the special case that transverse variations are absent ($\partial/\partial Y = 0$), (2.8a) and (2.8b) reduce to the steady nonlinear Schrödinger (NLS) equation which admits the well-known envelope-soliton solution with a 'sech' profile; one thus recovers the elevation and depression plane solitary waves that also bifurcate at $c = -1$.

To trace lump-solution branches, $\bar{\eta}(\chi, y; c)$ where $\chi = x - ct$, in the finite-amplitude range away from their bifurcation point, we solve directly the steady version of (2.2),

$$(-c\bar{\eta} + 3\bar{\eta}^2 + 2\bar{\eta}_{\chi\chi} + \bar{\eta}_{\chi\chi\chi\chi})_{\chi\chi} + \bar{\eta}_{yy} = 0, \tag{2.9}$$

via a Fourier-iteration method, analogous to the one used in Musslimani & Yang (2004), using 1024×128 modes along the horizontal and the transverse direction, in a computational domain $120\pi \times 60\pi$. Figure 2-1 shows the peak amplitude $\eta_0 = \bar{\eta}(\chi = 0, y = 0; c)$ of depression lumps (also known as the primary solution branch) as c is decreased below –1. Also, for comparison, we have plotted the peak amplitude of plane solitary waves of depression. Although, for the same speed, lumps have roughly twice the peak amplitude of solitary waves, the two solution branches behave in a similar manner qualitatively as c is varied; also lump profiles along the centreline $y = 0$ are similar to those of plane solitary waves. The computations of Parau *et al.* (2005, 2007) revealed an analogous behaviour for gravity–capillary lumps and solitary waves on water of finite or infinite depth.

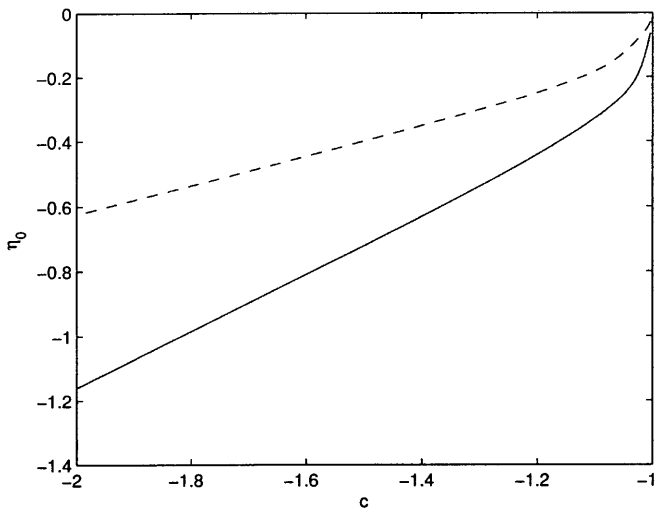

Figure 2-1: Peak amplitudes of lumps (solid) and plane solitary waves (dashed) of depression as the wave speed c is decreased below the bifurcation point $c = -1$.

On the other hand, considering that the ground state of the BRDS equations is prone to collapse while NLS envelope solitons are stable, one would expect the dynamics of lumps to be quite different from that of plane solitary waves. This issue is taken up below by first examining the stability of lumps to infinitesimal perturbations.

2.3 Exchange of stability

We shall focus on the primary (depression) lump-solution branch, $\bar{\eta}(\chi, y; c)$, parameterized by the wave speed c, of the fifth-order KP equation (2.2). Upon superposing a perturbation $\eta'(\chi, y, t)$ and linearizing about the basic state, η' satisfies

$$\{\eta'_t - c\eta'_\chi + 6(\bar{\eta}\eta')_\chi + 2\eta'_{\chi\chi\chi} + \eta'_{\chi\chi\chi\chi\chi}\}_\chi + \eta'_{yy} = 0. \tag{2.10}$$

Before considering the associated eigenvalue stability problem, in a preliminary stability analysis, we integrated the linearized perturbation equation (2.10) numeri-

cally by a spectral method that parallels the one used in Kim & Akylas (2006), for various values of c below the bifurcation point ($c = -1$), taking as initial condition $\eta'(\chi, y, t = 0) = \bar{\eta}(\chi, y; c)$. The spatial resolution was the same as that used earlier for the steady equation (2.9), and the time step $\Delta t = 5 \times 10^{-3}$. To monitor the evolution of the disturbance, we compute

$$E'(t) = \int_{-\infty}^{\infty} \int_{-\infty}^{\infty} \eta'^2 \mathrm{d}\chi \mathrm{d}y. \tag{2.11}$$

We first considered values of c slightly below -1, for instance $c = -1.02$, for which lump profiles resemble small-amplitude modulated wavepackets. Following an initial transient period, $\ln E'(t)$ eventually grows linearly with time, indicating exponential growth of $E'(t)$, and this trend also was confirmed by monitoring the growth of the peak amplitude of the disturbance with time. On the other hand, for values of c farther from the bifurcation point, for example $c = -1.64$, $E'(t)$ exhibits quite different behaviour: as suggested by a log–log plot of $E'(t)$ against t, eventually, $E'(t) \propto t^2$ so the disturbance now grows linearly with time. This is not a sign of instability, however, as it is easy to show that the perturbation equation (2.10) admits the linearly-growing disturbance $\eta' = t\bar{\eta}_\chi - \partial\bar{\eta}/\partial c$ as a solution, which may be interpreted as a shift in the speed parameter of the base state $\bar{\eta}(\chi, y; c)$. Consistent with this reasoning, the numerical results confirm that $\eta' \propto t\bar{\eta}_\chi$ at large time.

The overall picture suggested by these computations is that η' grows exponentially, implying instability, when $-1.053 < c < -1$. Figure 2-2 shows the computed growth rate λ for c in this range; as c is decreased below the bifurcation point, λ first increases until $c \approx -1.03$ where a maximum is reached, and then it decreases sharply. On the other hand, for $c < -1.09$, there is no evidence of instability as η' eventually grows linearly with time, $\eta' \propto t\bar{\eta}_\chi$. Finally, for c in the range $-1.09 < c < -1.053$, our numerical results are not entirely conclusive, and we suspect that the computation has to be carried out to very long times ($t > 200$) in order to see a definite trend in this transitional regime between unstable and stable behaviour.

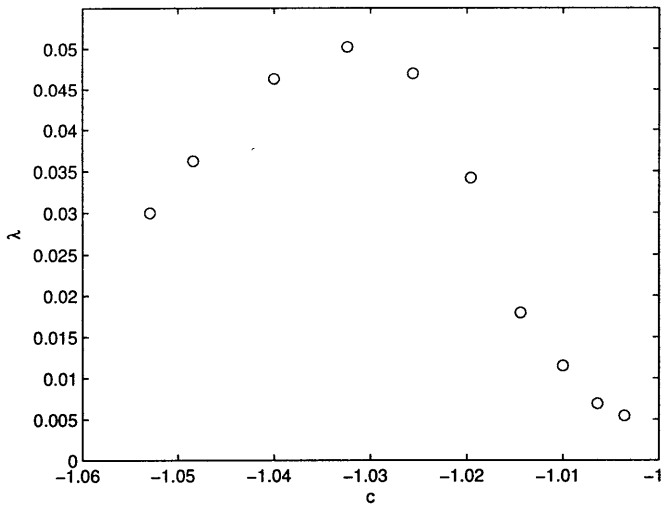

Figure 2-2: Numerically computed growth rate λ of the instability of depression lumps with wave speed in the range $-1.053 < c < -1$.

Turning next to a formal stability analysis, upon substituting $\eta' = \hat{\eta}(\chi, y)\exp(\lambda t)$ in (2.10), $\hat{\eta}$ is governed by

$$(\lambda\hat{\eta} - c\hat{\eta}_\chi + 6(\bar{\eta}\hat{\eta})_\chi + 2\hat{\eta}_{\chi\chi\chi} + \hat{\eta}_{\chi\chi\chi\chi\chi})_\chi + \hat{\eta}_{yy} = 0, \tag{2.12a}$$

$$\hat{\eta} \to 0 \quad (\chi^2 + y^2 \to \infty), \tag{2.12b}$$

assuming that the perturbations are locally confined. This defines an eigenvalue problem, the eigenvalues occurring in quartets (λ, $-\lambda$, λ^*, $-\lambda^*$); instability thus is associated with eigenvalues that are not purely imaginary.

In the light of the numerical results presented above, one would expect a pair of real eigenvalues when $-1.053 < c < -1$, as disturbances were found to grow exponentially for c in this range. Combined with the fact that no instability was detected when $c < -1.09$, this suggests that, for a certain c between -1.053 and -1.09, an exchange of stability takes place, the pair of real eigenvalues colliding at the origin $\lambda = 0$ as this critical value of c is approached from above.

To explore further this hypothesis, a bifurcation analysis near the possible onset of instability ($|\lambda| \ll 1$) was carried out, adapting to the case of lumps a procedure

suggested in Pelinovsky & Grimshaw (1997) for the stability of plane solitary waves. Specifically, introducing the expansion

$$\hat{\eta} = \hat{\eta}^{(0)} + \lambda\hat{\eta}^{(1)} + \lambda^2\hat{\eta}^{(2)} + \cdots, \tag{2.13}$$

$\hat{\eta}^{(0)}$ is posed as a linear combination of $\bar{\eta}_\chi$ and $\bar{\eta}_y$, $\hat{\eta}^{(0)} = \bar{\eta}_\chi + C\bar{\eta}_y$, which are solutions of (2.12a) and (2.12b) for $\lambda = 0$ by virtue of the invariance of $\bar{\eta}$ to translations in χ and y.

At $O(\lambda)$, $\hat{\eta}^{(1)}$ is governed by the forced equation $\mathcal{L}\hat{\eta}^{(1)} = -\bar{\eta}_{\chi\chi} - C\bar{\eta}_{\chi y}$, $\mathcal{L}$ denoting the linear operator in (2.12a) for $\lambda = 0$, and is subject to condition (2.12b) at infinity. The solution is expressed as

$$\hat{\eta}^{(1)} = -\frac{\partial\bar{\eta}}{\partial c} - C\left.\frac{\partial\tilde{\eta}}{\partial c_2}\right|_0, \tag{2.14}$$

where $\tilde{\eta}(\chi, y; c, c_2)$ satisfies

$$\left\{-c\tilde{\eta}_\chi - c_2\tilde{\eta}_z + 3(\tilde{\eta}^2)_\chi + 2\tilde{\eta}_{\chi\chi\chi} + \tilde{\eta}_{\chi\chi\chi\chi\chi}\right\}_\chi + \tilde{\eta}_{yy} = 0, \tag{2.15}$$

and $\partial\tilde{\eta}/\partial c_2|_0$ denotes $\partial\tilde{\eta}/\partial c_2$ evaluated for $c_2 = 0$. (As explained in Kim & Akylas (2006), physically $\tilde{\eta}$ corresponds to an oblique lump solution and can be mapped to a lump propagating along the x-direction via rotation of axes.)

Proceeding to $O(\lambda^2)$, it follows from (2.12a), making use of (2.14), that $\hat{\eta}^{(2)}$ satisfies

$$\mathcal{L}\hat{\eta}^{(2)} = \left(\frac{\partial\bar{\eta}}{\partial c} + C\left.\frac{\partial\tilde{\eta}}{\partial c_2}\right|_0\right)_\chi, \tag{2.16}$$

subject to condition (2.12b). Appealing to the usual solvability argument, for this inhomogeneous problem to have a solution, it is necessary that the right-hand side in (2.16) be orthogonal to the well-behaved homogeneous solution of the corresponding adjoint problem. Here, the operator adjoint to $\mathcal{L}$ is

$$\mathcal{L}^A = -c\,\partial_\chi^2 + 6\bar{\eta}\,\partial_\chi^2 + 2\partial_\chi^4 + \partial_\chi^6 + \partial_y^2, \tag{2.17}$$

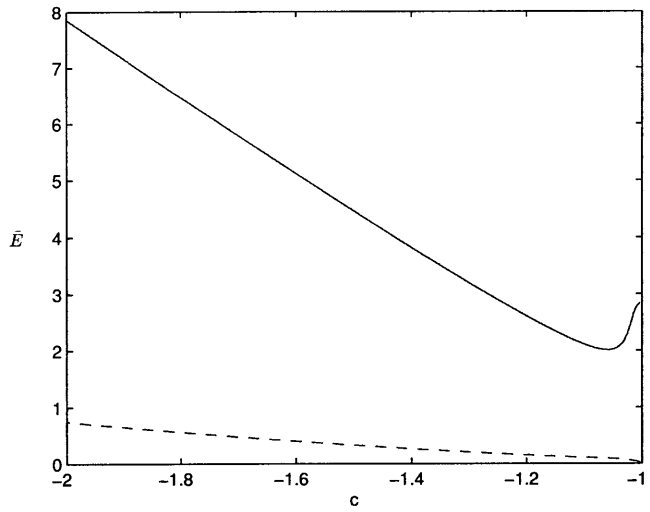

Figure 2-3: $\bar{E}(c)$ for lumps (solid) and plane solitary waves (dashed) of depression as the wave speed c is decreased below the bifurcation point $c = -1$.

and a well-behaved solution of $\mathcal{L}^A \eta^A = 0$ is readily shown to be

$$\eta^A = \int_{-\infty}^{\chi} \bar{\eta}\, \mathrm{d}\chi'. \tag{2.18}$$

(Note that $\eta^A \to 0$ as $\chi \to \infty$, as required by the well-known constraint of the KP equation; see, for example, Akylas (1994).) Imposing this solvability condition on the right-hand side of (2.16), making use of the fact that $\partial\tilde{\eta}/\partial c_2|_0$ is odd in χ and y, it follows that

$$\frac{\mathrm{d}\bar{\mathrm{E}}}{\mathrm{dc}} = 0, \tag{2.19}$$

where $\bar{E}(c) = \int_{-\infty}^{\infty}\int_{-\infty}^{\infty} \bar{\eta}^2 \mathrm{d}\chi \mathrm{d}y$. The constant C remains undetermined at this stage.

The above heuristic analysis, assuming that $\hat{\eta}^{(0)}$ is a linear combination of $\bar{\eta}_\chi$ and $\bar{\eta}_y$, suggests (2.19) as a necessary condition at the critical value of c where exchange of stability takes place. Figure 2-3 shows $\bar{E}(c)$ for the depression-lump solution branch computed earlier, along with a plot of $\bar{E}(c)$ (per unit y) for plane solitary waves of depression. It is interesting that $\bar{E}$ corresponding to depression lumps features a minimum, so (2.19) is met, at $c = -1.0576$, consistent with our numerical results (see figure 2-2) which indicate that exchange of stability occurs for a value of c in

the range $-1.09 < c < -1.053$. On the other hand, as shown in figure 2-3, $\bar{E}$ grows monotonically for plane solitary waves of depression, as they are stable to longitudinal perturbations (Calvo, Yang & Akylas 2000).

2.4 Transient evolution

The linear stability analysis presented above indicates that, close to their bifurcation, lumps are unstable to infinitesimal perturbations. Also when viewed as wavepackets, these small-amplitude lumps are on the verge of wave collapse according to the BRDS equations. Here we follow the transient evolution of linear instability in the nonlinear regime, in an attempt to understand the meaning of this singularity.

For this purpose, we solve the fifth-order KP equation (2.2) numerically as an initial-value problem, employing a spectral technique analogous to the one in Kim & Akylas (2006). The spatial resolution used is the same as before and $\Delta t = 1.0 \times 10^{-3}$. It can be readily shown that, for locally confined disturbances,

$$E = \int_{-\infty}^{\infty} \int_{-\infty}^{\infty} \eta^2(x, y, t) \mathrm{d}x \mathrm{d}y. \tag{2.20}$$

is conserved, and this property was also used to check the accuracy of the computations.

The first set of initial conditions considered is of the form

$$\eta = (1 + \delta)\bar{\eta}(x, y; c) \quad (t = 0), \tag{2.21}$$

where $\bar{\eta}$ denotes the depression-lump solution branch computed earlier and δ is a parameter that controls the amplitude and sign of the perturbation imposed. For c in the linearly stable range found in §2.3, for instance $c = -1.64$, we confirmed that lumps propagate stably under perturbations of either sign.

However, close to the bifurcation point $c = -1$, where lumps are linearly unstable and resemble small-amplitude wavepackets, the BRDS equations predict that the initial condition (2.21) would eventually either collapse (for $\delta > 0$) or disperse

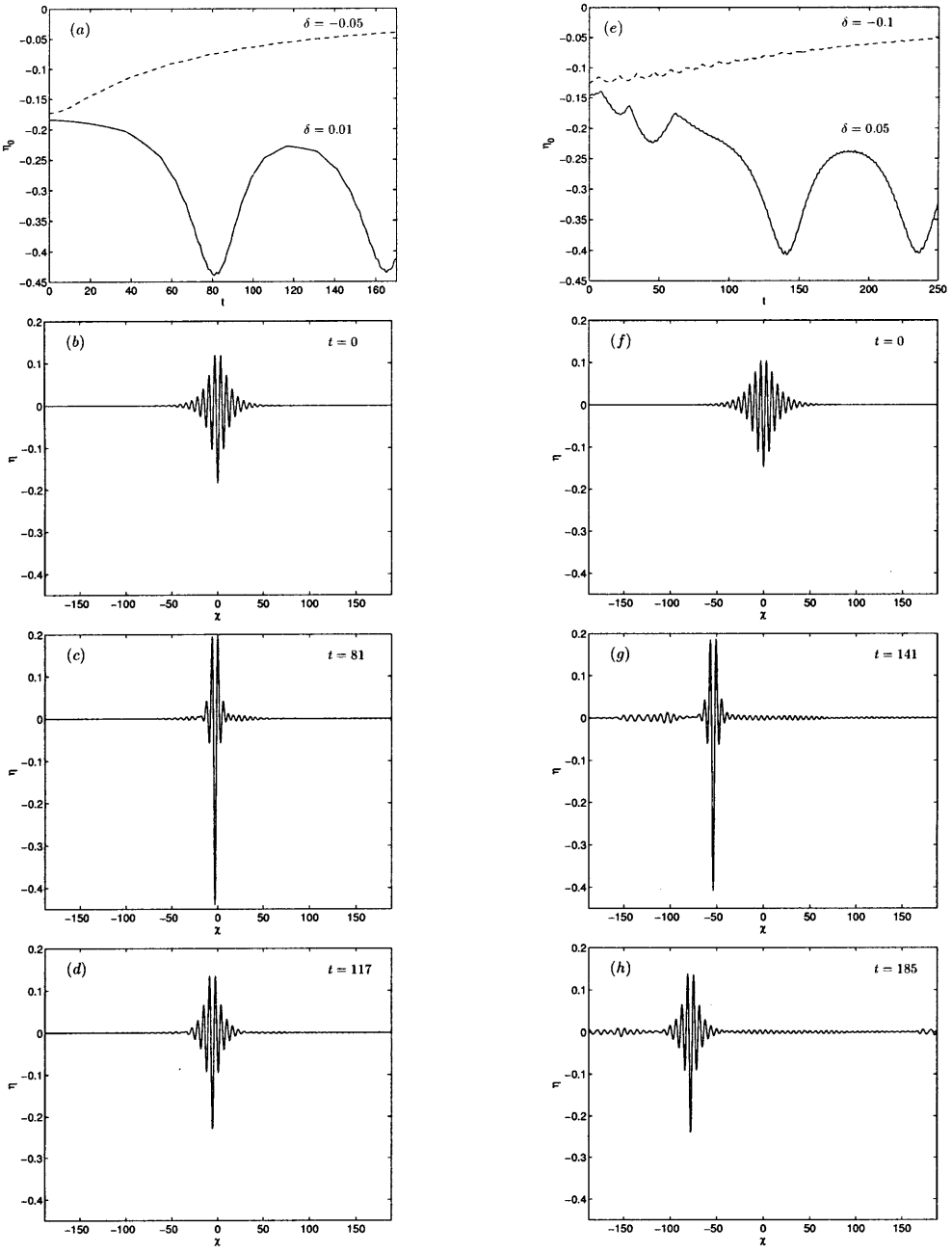

Figure 2-4: Results of numerical simulations using the initial condition (2.21). Left: $\bar{\eta}$ corresponds to lump with $c = -1.0225$; (a): peak-amplitude evolution for positive and negative perturbation; (b)–(d): centreline profiles in frame moving with c at selected times. Right: $\bar{\eta}$ is ground-state wavepacket with $k = 1.05$ and $\epsilon = 0.15$; (e): same as (a) above; (f)–(h): centreline profiles in frame moving with $c_g = -0.5375$ at selected times.

out (for $\delta < 0$). Figure 2-4(a–d) shows results from computations using the initial condition (2.21) for $c = -1.0225$, which is in the linearly unstable range (see figure 2-2). For a positive perturbation ($\delta = 0.01$), the peak amplitude of the disturbance initially grows, as expected from the results of the linear stability analysis, but rather than experiencing wave collapse as the BRDS equations would imply, the disturbance evolves to a finite-amplitude oscillatory state (figure 2-4a). Representative wave profiles, corresponding to the initial condition and to the times at which the (magnitude of the) peak amplitude reaches its first maximum and minimum are displayed in figure 2-4(b–d). The disturbance profile at the maximum of the peak amplitude (figure 2-4c) is close to the stable finite-amplitude lump that corresponds to $c \approx -1.17$ in figure 2-1.

On the other hand, for the same initial condition as above, but with negative perturbation ($\delta = -0.05$), the peak amplitude decreases in magnitude monotonically (see figure 2-4a), and the disturbance decays into dispersive waves. This is consistent with the BRDS equations which predict that initial conditions below the ground state ($\delta < 0$) eventually disperse out.

We next consider as initial condition a wavepacket with envelope given by the ground state of the BRDS equations, but with carrier wavenumber other than $k = k_m = 1$ corresponding to the minimum phase speed, so the initial disturbance as a whole is far from a lump. Specifically, we chose $k = 1.05$, which is still in the range $\sqrt{3/5} < k < \sqrt{6/5}$ where the BRDS equations (2.7) are of the elliptic–elliptic focusing type, and $\bar{\eta}$ in (2.21) was replaced by the first three harmonics in expansion (2.4), using the corresponding ground state $\bar{S}(X, Y)$ as the envelope S and $\epsilon = 0.15$.

The results of the evolution of this initial condition are summarized in figure 2-4(e–h). For a positive perturbation ($\delta = 0.05$), after an initial transient period, the peak amplitude of the disturbance again exhibits an oscillatory behaviour (figure 2-4e). Moreover, as illustrated in figure 2-4(f–h), rather than the wave collapse predicted by the BRDS equations when $\delta > 0$, the disturbance oscillates essentially between two depression lumps, one of relatively small amplitude ($\eta_0 \approx -0.24$) that is unstable and the other of higher amplitude ($\eta_0 \approx -0.41$) that is stable. Here, the results are dis-

played in a frame moving with the group velocity $c_g = -0.5375$ of the initial packet, so the main disturbance is seen to propagate to the left (figure 2-4(f–h)), as lumps propagate with speed less than -1. In contrast, the same initial wavepacket but with a negative perturbation ($\delta = -0.1$) results in a decaying disturbance (figure 2-4e) that eventually disperses out, as also predicted by the BRDS equations for $\delta < 0$.

These results have brought out the prominent role of finite-amplitude lumps in the nonlinear focusing of localized wavepackets. Extension of these ideas to the full water-wave problem, including the effects of damping and forcing, are topics in the following chapters (Chapter 3, Chapter 4).

Chapter 3

Forced Waves Near Resonance at a Phase-Speed Minimum

3.1 Introduction

In dispersive wave systems, maxima or minima of the linear phase speed are associated with the bifurcation of plane solitary waves, and a phase-speed minimum is also a possible bifurcation point of fully localized solitary waves, often called 'lumps' (see, for example, Grimshaw 2007). Moreover, when a wave system is subject to forcing by a moving external disturbance, the linear response exhibits resonance phenomena at a maximum or minimum of the phase speed due to the fact that the phase and group speeds are equal there. As a result, nonlinear effects can play an important part near such critical forcing speeds.

In the case that the phase speed features a maximum or minimum at zero wavenumber (long-wave limit), the forced problem near resonant conditions has been studied extensively in various physical contexts and is well understood. For two-dimensional (plane) forcing and ignoring dissipation, the weakly nonlinear response is governed in general by the forced Korteweg–de Vries (KdV) equation. This evolution equation predicts periodic shedding of solitary waves for a range of transcritical forcing speeds, consistent with observations (Akylas 1984; Grimshaw & Smyth 1986; Wu 1987). When the forcing is three-dimensional, the forced KdV equation is replaced by the

forced Kadomtsev–Petviashvili (KP) equation (Katsis & Akylas 1987), which admits lumps as free solutions only if the long-wave speed is a phase-speed minimum. In most physical examples, including gravity surface and internal waves, the long-wave speed is a maximum; it does happen to be a minimum, though, for gravity–capillary surface waves in the presence of strong surface tension (Bond number, $B > 1/3$), but this condition restricts the water depth to less than a few mm so ignoring viscous effects cannot be justified.

The present chapter is concerned with the resonant response when the linear phase speed features a minimum at a non-zero wavenumber. This case is more complicated and has received far less attention than the long-wave limit; here, a weakly nonlinear approach using a generic evolution equation, analogous to the forced KdV and KP equations, turns out to be not entirely satisfactory and, moreover, viscous dissipation effects cannot be ignored in general.

Most of prior related work was done for gravity–capillary surface waves, motivated by applications to the generation of ripples by wind (Zhang 1995) and the wave drag of moving bodies on a free surface (Raphaël & De Gennes 1996; Burghelea & Steinberg 1996). However, phase-speed minima also arise and resonance is possible in the response of a floating ice sheet to surface loads, the role of capillarity being taken in this instance by the flexural rigidity of the ice (Squire *et al.* 1996), as well as in layered flows that support 'gap' solitons (Grimshaw & Malomed 1994).

For free gravity–capillary waves, according to potential-flow theory, the linear phase speed features a minimum, $c_{\min}$, at non-zero wavenumber when $B < 1/3$, and this is possible on water of finite or infinite depth (eg, in deep water, $c_{\min} = 23.2\text{cm/s}$ with corresponding wavelength $\lambda_{\min} = 1.71\text{cm}$). At $c_{\min}$ bifurcate two symmetric plane solitary-wave solutions of the wavepacket type, the so-called elevation and depression branches. These have been studied analytically in the small-amplitude limit as well as numerically for finite steepnesses (see the review Dias & Kharif 1999). It turns out that weakly nonlinear elevation and depression solitary waves can be approximated as envelope solitons with stationary crests in terms of the nonlinear Schrödinger (NLS) equation (Akylas 1993; Longuet-Higgins 1993); but the NLS equa-

tion alone is not able to predict the various other solitary wave solutions that bifurcate at finite amplitude below $c_{\min}$ (Yang & Akylas 1997).

In regard to the forced gravity–capillary problem, Vanden-Broeck and Dias (1992) computed, on the basis of potential flow, the steady-state wave response due to a one-dimensional symmetric pressure disturbance of finite extent moving on the surface of deep water. Starting at a subcritical forcing speed far below $c_{\min}$ with the small-amplitude locally confined response predicted by linear theory (known as Rayleigh's solution), they followed this solution branch via numerical continuation, gradually increasing the forcing speed. Rather than blowing up at $c_{\min}$ as linear theory would suggest, Rayleigh's solution branch turns around at a certain critical speed, forming a limit point before $c_{\min}$ is reached, and then follows a finite-amplitude subcritical solution branch close to free depression solitary waves.

Calvo & Akylas (2002) examined the linear stability of this steady-state subcritical forced response and concluded that only the small-amplitude branch is stable, suggesting that Rayleigh's solution would be realizable. What happens for forcing speeds past the limit point brought out by the computations, however, is not clear. In a related experimental study, Longuet-Higgins & Zhang (1997) used an air jet from a narrow slit as forcing over a current in deep water. The observed responses for a range of subcritical current speeds close to $c_{\min}$, while locally confined, were accompanied by persistent unsteadiness. According to estimates (Calvo & Akylas 2002), the forcing speeds in these experiments were probably higher than the critical speed corresponding to the limit point of the steady-state response.

Apart from unsteady effects, viscous dissipation, too, apparently plays an important part in the forced response near resonant conditions. While viscous dissipation alone is capable of healing the singular behavior of the linear response at $c_{\min}$ (Richard & Raphaël 1999), the interplay of viscous dissipation and nonlinearity can have a rather dramatic effect, according to computations by Kang & Vanden-Broeck (2005). When viscous dissipation is not too strong, in particular, numerical continuation along the small-amplitude subcritical solution branch reveals a rich response structure, with multiple branches of nonlinear steady states being possible as $c_{\min}$ is

approached from below; whether or not these states are realizable is unclear, however. In addition, there is evidence that viscous dissipation is important in the response of ice sheets to moving loads near the minimum gravity–flexural phase speed. Rather than being symmetric about the load position as predicted by inviscid nonlinear computations (Parau & Dias 2002), the response recorded in field observations (Takizawa 1988; Squire *et al.* 1988) for subcritical speeds is markedly asymmetric, consistent with a viscoelastic model (Hosking *et al.* 1988).

In an effort to address some of the issues raised above, the present chapter focuses on a simple model dispersive wave system with a phase-speed minimum at non-zero wavenumber, namely, a forced–damped fifth-order KdV equation. In the absence of forcing and viscous dissipation, this model has also proven useful in understanding free solitary waves of the wavepacket type that bifurcate in the vicinity of a minimum of the phase speed (Yang & Akylas 1997). Here, emphasis is placed on the combined effect of forcing, nonlinearity and viscous dissipation in the response near resonant conditions.

3.2 Steady response: perturbation results

The ensuing analysis is based on a fifth-order KdV equation with the addition of viscous dissipation and forcing. In normalized form, combining a Burgers-type viscous dissipation term with locally confined forcing traveling along x with speed V, this equation reads

$$\eta_t - V\eta_\xi + 6\eta\eta_\xi + 2\eta_{\xi\xi\xi} + \eta_{\xi\xi\xi\xi\xi} - \nu\eta_{\xi\xi} = Ap_\xi, \tag{3.1}$$

in the reference frame following the forcing, $\xi = x - Vt$. The parameters $\nu \geq 0$ and A control the strength of viscous dissipation and forcing, respectively.

The fifth-order KdV equation can be formally derived from the full potential-flow equations for gravity–capillary waves, assuming weakly nonlinear long disturbances for Bond number B close to $1/3$. However, as remarked earlier, the condition $B \approx 1/3$ severely limits the applicability of this equation to surface waves because boundary layer effects from the bottom cannot be neglected in this flow regime. Here, equation

(3.1) is viewed merely as a convenient model problem, that features a phase-speed minimum at non-zero wavenumber and also combines nonlinearity, viscous dissipation and forcing in a rather simple way.

We begin by looking at the steady-state response $\eta^s(\xi; V)$. Ignoring the nonlinear term in (3.1), the linearized steady state is readily found by Fourier transform:

$$\eta^s = A \int_{-\infty}^{\infty} \frac{\hat{p}(k) e^{ik\xi}}{\mathcal{D}(k; V, \nu)} dk, \tag{3.2}$$

where

$$\mathcal{D} = k^4 - 2k^2 - i\nu k - V \tag{3.3}$$

and

$$\hat{p}(k) = \frac{1}{2\pi} \int_{-\infty}^{\infty} p(\xi) e^{-ik\xi} d\xi. \tag{3.4}$$

The form of expression (3.2) is typical of the forced response due to a moving disturbance in dispersive wave systems (see, for example, Whitham 1974). As is well known, the behavior in the far field hinges on the zeros of $\mathcal{D}$ in the k-domain, as they correspond to the wavenumbers of free waves that can remain steady relative to the forcing. Mathematically, these zeros are also poles of the integrand in the complex k-plane and provide the main contribution in the far field upon evaluating the Fourier integral in (3.2).

According to the linear dispersion relation of equation (3.1), the phase speed of undamped ($\nu = 0$) propagating waves has a minimum, $c_{\min} = -1$, when $k = k_{\min} = 1$. For subcritical forcing speed ($V < -1$), the zeros of $\mathcal{D}$ thus turn out to be complex and the far-field response is evanescent, $\eta^s \to 0$ ($\xi \to \pm\infty$). On the other hand, for supercritical forcing speed ($V > -1$), $\mathcal{D} = 0$ has real roots in the absence of viscous dissipation ($\nu = 0$), corresponding to poles on the real k-axis in (3.2) and propagating waves in the far field. Letting $\nu > 0$, these poles are pushed off the real axis, which makes it possible to evaluate the integral in (3.2). It transpires that short waves (relative to $k_{\min}$) are found in $\xi > 0$ and long waves in $\xi < 0$, consistent with the radiation condition based on the group velocity (Whitham 1974).

The case of interest here is when the forcing speed V is near the phase-speed minimum, $c_{\min} = -1$. In this instance, the steady-state response (3.2) exhibits resonant behavior, similarly to a harmonic oscillator forced near its natural frequency. In the absence of viscous dissipation ($\nu = 0$), exactly at the critical forcing speed $V = -1$, $\mathcal{D}$ has a double root at $k = 1$, which translates into a double pole of the integrand in (3.2); as a result, η_s turns out to be singular. A more detailed analysis, based on an initial-value problem (Akylas 1984), indicates that the resonant response in fact grows unbounded with time, like $t^{1/2}$. This is easy to understand on physical grounds, as the group speed is equal to the phase speed at an extremum of the phase speed; hence, when $V = c_{\min}$, energy cannot be radiated away from the vicinity of the forcing, causing the response to grow.

While viscous dissipation alone does heal the singularity of the linear steady-state response at the critical speed $V = -1$ by pushing off the real axis the pole of the integrand, nonlinearity, too, is likely to be important near resonant conditions. In the vicinity of the critical speed, it is possible to set up a weakly nonlinear theory, similar to that presented in Calvo & Akylas (2002) for forced gravity–capillary waves, which would lead to a forced NLS equation with an additional term due to weak viscous dissipation. This approach, however, as it is valid when the response is of small amplitude, cannot describe the finite-amplitude subcritical steady-state response branches revealed by the computations cited earlier (Vanden-Broeck & Dias 1992; Kang & Vanden-Broeck 2005). To account for these solutions, here we shall explore the possibility of finite-amplitude steady responses in the form of free solitary waves, slightly modified by the presence of forcing and viscous dissipation.

In preparation for the perturbation analysis, we write

$$\eta^s(\xi; V) = \bar{\eta}(\xi + \theta; V) + A\tilde{\eta}, \tag{3.5}$$

where $\bar{\eta}$ denotes an undamped free solitary-wave solution of (3.1) traveling with speed V, that satisfies

$$-V\bar{\eta} + 3\bar{\eta}^2 + 2\bar{\eta}_{\xi\xi} + \bar{\eta}_{\xi\xi\xi\xi} = 0, \tag{3.6}$$

and θ denotes a phase-shift constant to be found. Since solitary waves are found below the phase-speed minimum, it is implicitly assumed here that V is in the subcritical range, $V < -1$. We also write

$$\nu = \mu A, \tag{3.7}$$

μ being a parameter that measures the strength of viscous dissipation relative to forcing. (We shall take $A > 0$, implying that $\mu \geq 0$ since $\nu \geq 0$.)

Upon substituting (3.5) into (3.1), making use of (3.6) and (3.7), it is then found that the perturbation $\tilde{\eta}$ is governed by the equation

$$-V\tilde{\eta} + 6\bar{\eta}(\xi + \theta; V)\tilde{\eta} + 2\tilde{\eta}_{\xi\xi} + \tilde{\eta}_{\xi\xi\xi\xi} = \mu\bar{\eta}_{\xi} + p(\xi) + A(\mu\tilde{\eta}_{\xi} - 3\tilde{\eta}^2). \tag{3.8}$$

Equation (3.8) is solved by expanding $\tilde{\eta}$ and θ in powers of $0 < A \ll 1$:

$$\tilde{\eta} = \tilde{\eta}^{(0)} + A\tilde{\eta}^{(1)} + \cdots, \quad \theta = \theta_0 + A\theta_1 + \cdots. \tag{3.9}$$

To leading order, $\tilde{\eta}^{(0)}$ satisfies the forced equation

$$-V\tilde{\eta}^{(0)} + 6\bar{\eta}(\xi + \theta_0; V)\tilde{\eta}^{(0)} + 2\tilde{\eta}^{(0)}_{\xi\xi} + \tilde{\eta}^{(0)}_{\xi\xi\xi\xi} = \mu\bar{\eta}_{\xi}(\xi + \theta_0; V) + p(\xi). \tag{3.10}$$

Note that the differential operator in (3-10) is self-adjoint and, from (3.6), $\bar{\eta}_{\xi}(\xi+\theta_0; V)$ is a homogeneous solution that decays to zero as $\xi \to \pm\infty$. Appealing then to the usual solvability argument, in order for (3.10) to have a well-behaved solution at infinity, it is necessary that the forcing be orthogonal to $\bar{\eta}_{\xi}(\xi + \theta_0; V)$:

$$\mu\int_{-\infty}^{\infty} \bar{\eta}_{\xi}(\xi; V)^2 d\xi + \int_{-\infty}^{\infty} p(\xi)\bar{\eta}_{\xi}(\xi + \theta_0; V) d\xi = 0. \tag{3.11}$$

The solvability condition (3.11) provides an equation for determining the phase shift θ_0. In the absence of viscous dissipation ($\mu = 0$) and for symmetric forcing $p(\xi)$ about $\xi = 0$, $\theta_0 = 0$ is always a possible solution, corresponding to a symmetric forced response, consistent with inviscid computations of forced gravity–capillary waves (Vanden-Broeck & Dias 1992). When viscous dissipation is present ($\mu > 0$),

however, θ_0 is no longer zero, and the response (3.5) is asymmetric, the solitary wave $\bar{\eta}$ being shifted relative to $\xi = 0$.

To see the effect of viscous dissipation more clearly, take

$$p(\xi) = -\delta(\xi), \tag{3.12}$$

in which case condition (3.11) simplifies to

$$\bar{\eta}_\xi(\theta_0; V) = \mu \int_{-\infty}^{\infty} \bar{\eta}_\xi(\xi; V)^2 d\xi. \tag{3.13}$$

Now, the solitary-wave profile $\bar{\eta}(\xi; V)$ does not depend on μ, and $\bar{\eta}_\xi$ oscillates between positive and negative values. Hence, for given V, one would be able to satisfy (3.13) only if viscous dissipation is not too strong, $\mu < \mu_{\text{crit}}$; and, for each $\mu < \mu_{\text{crit}}$, more than one solutions θ_0 would be expected.

Having determined θ_0 and $\tilde{\eta}^{(0)}$, it is straightforward to find corrections by proceeding to higher order in the perturbation expansions (3.9). Specifically, applying a similar solvability condition to the $O(A)$ problem for $\tilde{\eta}^{(1)}$ yields

$$-6\theta_1 \int_{-\infty}^{\infty} \tilde{\eta}^{(0)} \bar{\eta}_\xi(\xi + \theta_0; V)^2 d\xi + \int_{-\infty}^{\infty} \{\mu \tilde{\eta}_\xi^{(0)} - 3(\tilde{\eta}^{(0)})^2\} \bar{\eta}_\xi(\xi + \theta_0; V) d\xi = 0; \tag{3.14}$$

this readily specifies θ_1.

The results of the perturbation theory provide evidence that, when viscous dissipation is not too strong in comparison with forcing ($\mu < \mu_{\text{crit}}$), multiple finite-amplitude steady responses are possible for subcritical forcing speeds. These responses are essentially free solitary waves, slightly modified due to the presence of forcing and viscous dissipation. The main effect of viscous dissipation is to shift the position of the solitary wave relative to the forcing, and more than one value for this shift can be found corresponding to the same solitary-wave profile. Detailed comparison against numerical computations is carried out in §3.3 below.

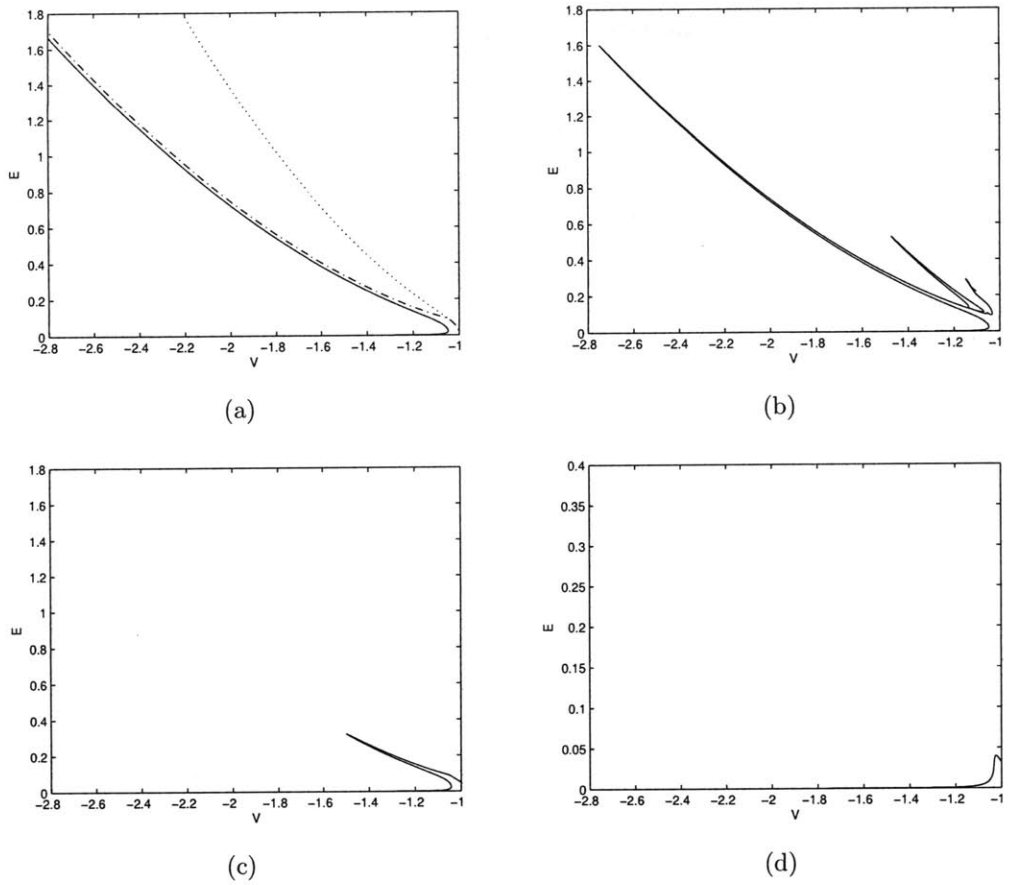

Figure 3-1: Steady-state response: E defined in (3.17) is plotted against V in the subcritical-speed range $V < -1$, for different values of the viscous dissipation parameter ν. (a) $\nu = 0$; (—) forced response; (-·-·-) free depression solitary waves; $(\cdots)$ free elevation solitary waves. (b) $\nu = 0.01$. (c) $\nu = 0.02$. (d) $\nu = 0.03$.

3.3 Steady response: numerical results

The steady version of equation (3.1),

$$-V\eta^s + 3\eta^{s2} + 2\eta^s{}_{\xi\xi} + \eta^s{}_{\xi\xi\xi\xi} - \nu\eta^s{}_{\xi} = Ap, \tag{3.15}$$

was integrated numerically for symmetric locally confined forcing in the form of a Gaussian:

$$p(\xi) = -\sqrt{\frac{10}{\pi}}e^{-10\xi^2}. \tag{3.16}$$

Equation (3.15) was discretized by second-order centered finite differences, using 1024 grid points in the computational domain $-150 < \xi < 150$, and solution branches were traced via pseudoarclength continuation. In all the computations, $A = 0.01\sqrt{\pi} = 0.0177$.

We first explore the combined effect of nonlinearity and viscous dissipation on Rayleigh's subcritical solution branch. Starting at a subcritical value of the forcing speed V well below $c_{\min} = -1$ with the small-amplitude response predicted by linear theory (Rayleigh's solution), we followed this branch as V was increased, for different values of the viscous dissipation parameter ν. The results of these computations are summarized in Figure 3-1, which shows plots of

$$E = \int_{-\infty}^{\infty} \eta^{s2} d\xi \tag{3.17}$$

against V for four values of ν.

Figure 3-1a, in particular, displays the undamped ($\nu = 0$) response which, as was found by Vanden-Broeck & Dias (1992), forms a limit point (at $V = -1.048$) before reaching $c_{\min}$ and then follows a finite-amplitude solution branch close to free solitary waves of depression. As expected, in the absence of viscous dissipation, the response is symmetric about $\xi = 0$, as is the forcing (3.16).

However, as illustrated in Figure 3-1b for $\nu = 0.01$, viscous dissipation can alter the undamped response diagram dramatically. Continuing Rayleigh's solution branch past the first limit point at $V = -1.047$, the response follows a finite-amplitude branch close to that of depression solitary waves as in the undamped case, but then turns around at $V \approx -2.75$, forming a second limit point, and heads towards $c_{\min}$ along a nearby branch. Continuing further, the reponse again turns away from $c_{\min}$, follows a different finite-amplitude branch, forms another limit point at $V \approx -1.5$ and returns to the vicinity of $c_{\min}$ once more. Interestingly, this second finite-amplitude solution branch is close to that of free elevation solitary waves, that also bifurcate at $c_{\min}$ (see Figure 3-1a).

For relatively stronger viscous dissipation ($\nu = 0.02$), Rayleigh's solution branch

follows a less complicated path upon continuation, as indicated in Figure 3-1*c*. However, nonlinearity still is a key factor, and the response is qualitatively similar to that of a forced lightly damped oscillator with a nonlinear spring close to resonance. Finally, upon increasing ν further, viscous dissipation eventually dominates over nonlinear effects, and the response diagram for $\nu = 0.03$ features merely a small peak near the critical speed, similarly to a forced damped linear oscillator in the vicinity of its resonance frequency (Figure 3-1*d*).

Although not immediately evident, the results displayed in Figure 3-1 are qualitatively similar to the computations of Kang & Vanden-Broeck (2005) for forced gravity–capillary waves in the presence of viscous dissipation. Note that they presented their results in terms of the free-surface displacement at the center point ($\xi = 0$) of the applied pressure forcing, rather than E defined in (3.17); when our results are re-plotted in terms of $\eta(0)$, they show similar behavior to theirs.

Returning now to Figure 3-1*b*, it is interesting that the forced response, in the presence of light viscous dissipation ($\nu = 0.01$), features two nearly identical finite-amplitude solution branches close to solitary waves of depression, and the same is true for the two branches neighboring solitary waves of elevation. This turns out to be a result of the combined effect of light forcing and viscous dissipation on solitary waves, and is consistent with the perturbation analysis in §3.2. As a check, consider the depression solitary wave for $V = -2.4$. With the approximation $p(\xi) \approx -\delta(\xi)$ of the forcing (3.16), and for $\mu = \nu/A = 1/\sqrt{\pi}$, corresponding to $\nu = 0.01$ and $A = 0.01\sqrt{\pi}$, the solvability condition (3.13) furnishes two possible values of the shift, $\theta_0 = 0.8$ and $\theta_0 = 1.7$. In line with these theoretical predictions, the two numerically computed forced response profiles at $V = -2.4$ are nearly identical to the depression solitary wave with the same speed, and are centered at $\xi = -0.88$ and $\xi = -1.77$. Moreover, varying V for fixed $\mu = 1/\sqrt{\pi}$, we find that condition (3.13) can be satisfied for $V > -2.8$, in reasonable agreement with the limit point at $V \approx -2.75$ computed numerically (Figure 3-1*b*).

The perturbation theory was also applied to solitary waves of elevation in order to make comparison with the forced responses found close to these solitary waves in

Figure 3-1*b*. Specifically, for $V = -1.4$ and again $\mu = \nu/A = 1/\sqrt{\pi}$, the solvability condition (3.13) now suggests four possible choices for the shift: $\theta_0 = -2.2$, -0.9, 4.1 and 4.9. The two positive values of θ_0 are consistent with the results in Figure 3-1*b*: the computed profiles at $V = -1.4$ closely resemble the elevation solitary wave having this speed, and are centered at $\xi = -4.1$ and $\xi = -5.0$. In addition, we were able to converge on two other forced responses close to the elevation solitary wave with $V = -1.4$, that were centered at $\xi = 0.88$ and $\xi = 2.36$; apparently, these correspond to the two negative values of the shift θ_0 predicted by the perturbation theory, but lie on subcritical solution branches that are not continuously connected to Rayleigh's solution.

3.4 Transient response

As remarked earlier, in the gravity–capillary problem, linear stability analysis of the inviscid steady-state response for subcritical forcing speeds indicates that the small-amplitude solution branch (Rayleigh's solution) is stable, while the finite-amplitude branch is unstable (Calvo & Akylas 2002). This would seem reasonable intuitively, as the latter solution branch corresponds to virtually free depression solitary waves, that a small perturbation would easily dislodge from the vicinity of the forcing. While no formal stability analysis will be pursued here, on similar physical grounds, one would also expect to be unstable the finite-amplitude steady states found in the presence of light viscous dissipation (Figure 3-1*b*). This then brings up the question as to the fate of the response for forcing speeds past the limit point of Rayleigh's solution.

To address this issue, we explored the transient response from rest through a numerical study of equation (3.1), subject to the forcing (3.16) with again $A = 0.01\sqrt{\pi}$, for various subcritical forcing speeds V and different values of the viscous dissipation parameter ν. Equation (3.1) was integrated by a Fourier spectral method in ξ combined with leap-frog time stepping, in the computational domain $-300 < \xi < 300$, using 2048 grid points and time step $\Delta t = 10^{-4}$.

According to the numerical results, the transient response from rest approaches

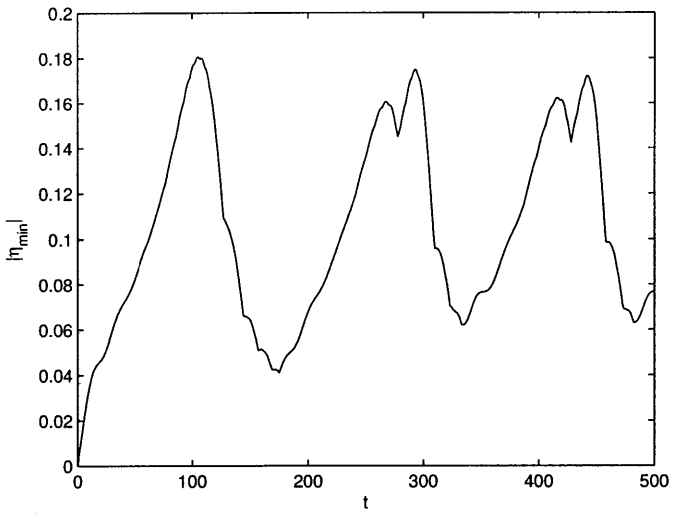

Figure 3-2: Plot against time of $|\eta_{\min}|$, the magnitude of η at the deepest trough, in the transient response from rest for $V = -1.02$ and $\nu = 0.01$. Under these conditions, Rayleigh's steady state is not available, and a time-periodic state is reached instead.

Rayleigh's small-amplitude steady solution when this state is available; this happens to be the case for all forcing speeds when viscous dissipation dominates (Figure 3-1d). However, for light to moderate viscous dissipation, Rayleigh's solution branch turns around, forming a limit point before reaching $V = -1$ (Figure 3-1(b, c)). The behavior of the transient response for forcing speed past the limit point then is determined by the strength of viscous dissipation, controlled by ν.

Consider first $\nu = 0.01$, corresponding to light damping. For this value of ν, according to Figure 3-1b, several finite-amplitude subcritical branches coexist with Rayleigh's steady state. The time-evolution of the transient response from rest for subcritical speeds past the limit point of Rayleigh's state ($V = -1.047$) is illustrated in Figure 3-2, which shows a plot of $|\eta_{\min}|$, the magnitude of η at the deepest trough, against time for $V = -1.02$. Following an initial period of continous growth, a maximum is reached at $t \approx 100$, and subsequently the response settles into a nonlinear time-periodic state that involves shedding of wavepacket solitary waves. Figure 3-3 shows snapshots of the disturbance at three instants within a cycle: at $t = 300$ (Figure 3-3a), the response is quite steep in the vicinity of the forcing and a solitary wave is

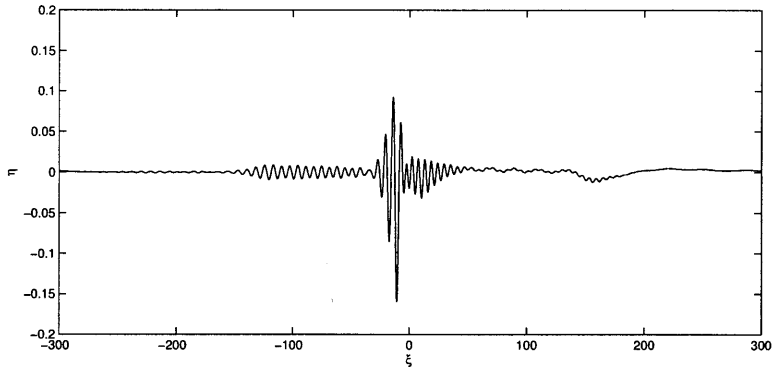

(a)

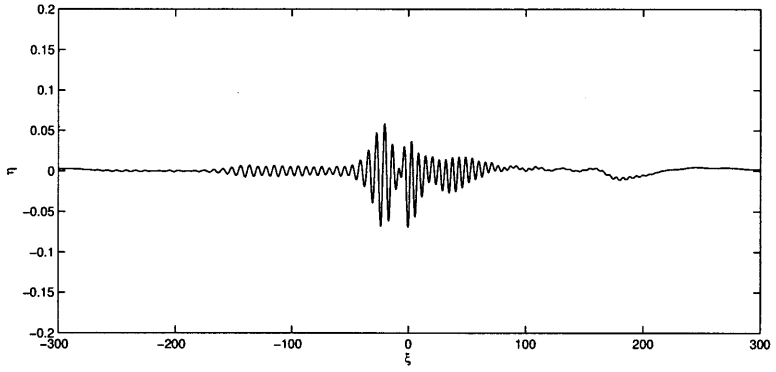

(b)

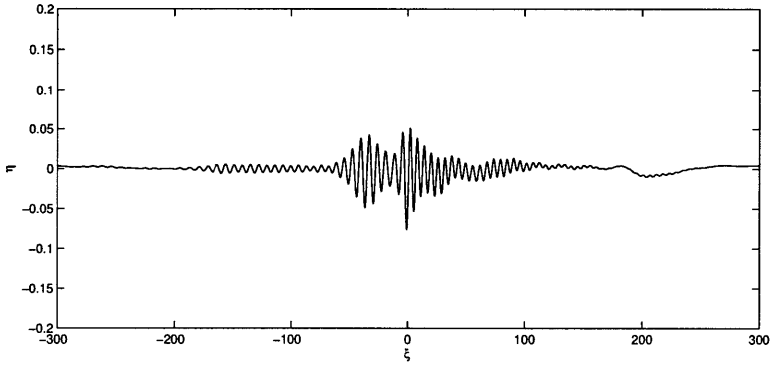

(c)

Figure 3-3: Three snapshots of time-periodic response for $V = -1.02$ and $\nu = 0.01$, illustrating the shedding of solitary waves. (a) $t = 300$. (b) $t = 325$. (c) $t = 350$.

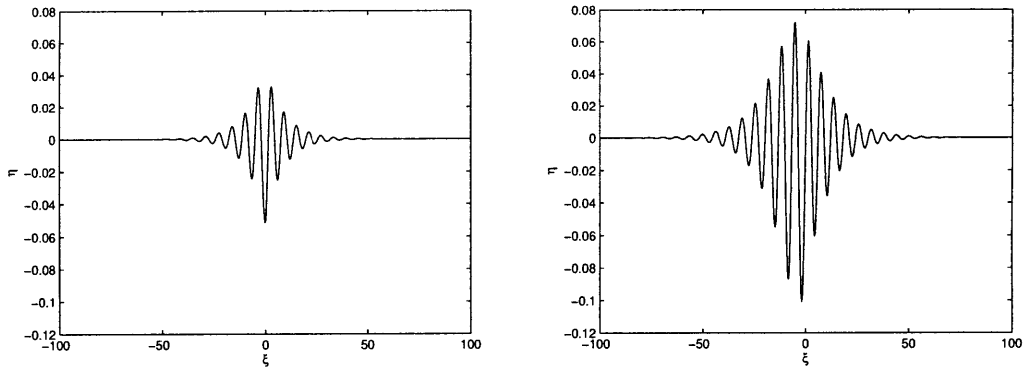

(a) (b)

Figure 3-4: Transient response from rest for $\nu = 0.02$. Profiles reached at steady state for forcing speed V slightly below and above the limit point of Rayleigh's solution at $V = -1.043$. (a) $V = -1.05$. (b) $V = -1.03$.

getting ready to be shed in $\xi < 0$; by $t = 325$, the solitary wave has clearly separated from the forcing (Figure 3-3*b*); and at $t = 350$, the effect of viscous dissipation on the solitary wave is already evident, as the disturbance near the forcing is starting to steepen again, in preparation for generating a new solitary wave (Figure 3-3*c*). Continuous shedding of solitary waves under these conditions of light damping seems consistent with the claim made earlier that finite-amplitude steady states close to free solitary waves are unstable to perturbations.

Increasing viscous dissipation to $\nu = 0.02$, Rayleigh's steady response again forms a limit point (Figure 3-1*c*), but the transient response from rest now reaches steady state for all subcritical forcing speeds. As the limit point at $V = -1.043$ is crossed, however, the response jumps from Rayleigh's solution to the solution branch present for forcing speeds above the limit point. This is illustrated in Figure 3-4 by the response profiles reached at steady state for $V = -1.05$ and $V = -1.03$, which are also in good agreement with those computed earlier by numerical continuation. Note that the response for $V = -1.03$ is noticeably asymmetric relative to the forcing and significantly steeper than the one for $V = -1.05$. Similar jump phenomena are encountered in the forced response of a lightly damped oscillator with a nonlinear spring near resonance.

3.5 Discussion

Based on the forced–damped fifth-order KdV equation studied here, the resonant response near a minimum of the phase speed at a non-zero wavenumber shares some common features with, but also has significant differences from, its counterpart at a phase-speed minimum or maximum in the long-wave limit. Both these phase-speed extrema are bifurcation points of free solitary waves and, moreover, define critical speeds at which the undamped linear forced response due to a moving disturbance exhibits resonant behavior. The nonlinear steady-state response near a phase-speed minimum at a non-zero wavenumber, however, has far more rich structure: multiple finite-amplitude solution branches are possible in the subcritical speed range, and light viscous dissipation can have a dramatic effect, as suggested by our perturbation analysis and numerical computations.

These subcritical finite-amplitude steady states, nonetheless, have little bearing on the transient response from rest, as it approaches the small-amplitude steady solution predicted by linear theory (Rayleigh's solution), if this state is available. Furthermore, for forcing speed close to critical, where the small-amplitude steady state may cease to exist, the fate of the transient response is determined by the strength of viscous dissipation in comparison with forcing. In the presence of relatively light viscous dissipation, in particular, a time-periodic state involving shedding of solitary waves is reached. This scenario is entirely analogous to the familiar periodic shedding of KdV solitary waves for transcritical forcing speeds in the long-wave limit. On the other hand, for stronger viscous dissipation, the transient response reaches steady state, but jump phenomena are possible. Given that the forcing speeds in the experiment of Longuet-Higgins & Zhang (1997) apparently were in a range where Rayleigh's solution was not available, it is tempting to speculate that the observed unsteadiness was related to shedding of solitary wavepackets.

It is interesting to note that the forced NLS equation, which can be derived asymptotically close to the critical forcing speed on the assumption of weakly nonlinear disturbances, also predicts the possibility of approaching a time-periodic state (Calvo

& Akylas 2002). However, according to the forced NLS equation, even with the addition of a viscous dissipation term, the response (in terms of the wave envelope) is symmetric relative to the forcing, whereas solitary wavepackets are shed only on one side of the forcing according to the full governing equation (Figure 3-3). Furthermore, the forced NLS equation cannot account for finite-amplitude steady responses.

In this chapter, the emphasis was on the resonant response for subcritical forcing speeds, and only the case of two-dimensional forcing was considered. In three dimensions, wavepacket solitary waves are replaced by lumps which, however, are stable only above a certain finite steepness (Akylas & Cho 2008; Chapter 2). The resonant response due to fully locally confined forcing, where these lumps could play a role, is investigated in the following chapter (Chapter 4).

Chapter 4

Resonantly forced gravity–capillary lumps on deep water

4.1 Introduction

Since the first observation of a two-dimensional (plane) gravity solitary wave of elevation by John Scott Russell, most attention has been paid to solitary waves on shallow water, that bifurcate from a uniform stream at the linear-long-wave speed and are governed by the Korteweg–de Vries (KdV) equation in the small-amplitude limit (Whitham 1974, §13.11). Apart from being the bifurcation point of KdV solitary waves, the long-wave speed, c_0, is also associated with a resonance condition: the linear response to external forcing moving at this critical speed grows unbounded in time (Akylas 1984). Naturally, nonlinear effects are important near this resonance, and the forced response due to a pressure disturbance on the free surface or a bottom bump travelling with speed close to c_0, involves periodic shedding of KdV solitary waves (Akylas 1984; Cole 1985; Wu 1987).

The KdV equation applies to two-dimensional (plane) waves and is replaced by the Kadomtsev–Petviashvili (KP) equation when variations in the transverse direction are taken into account (see, for example, Akylas 1994). The KP equation reveals that fully localized 3-D solitary waves, or 'lumps', are not possible on shallow water under typical flow conditions. On physical grounds, for a lump to remain locally

confined, its speed must be such that no linear wave can co-propagate with the main wave core; this is feasible when the speed at which lumps bifurcate coincides with a minimum of the linear phase speed, lumps thus being found below this minimum. In shallow water, however, c_0 is a maximum of the phase speed of pure gravity waves. For gravity–capillary waves, c_0 becomes a phase-speed minimum if surface tension σ is sufficiently strong: $\sigma > \frac{1}{3}\rho g H^2$, H being the water depth, ρ the fluid density and g the gravitational acceleration; but this condition restricts H to less than a few mm.

The situation is entirely different for gravity–capillary waves on deep water. Ignoring viscous dissipation, the phase speed now features a minimum, $c_{\min} = \sqrt{2}(\sigma g/\rho)^{1/4}$, at the non-zero wavenumber $k_{\min} = (\rho g/\sigma)^{1/2}$. (In cgs units, $\sigma = 73$, $\rho = 1$ and $g = 981$, so $c_{\min} = 23$ cm/s and $\lambda_{\min} = 2\pi/k_{\min} = 1.71$ cm.) This minimum is the bifurcation point of a new class of plane gravity-capillary solitary waves as well as lumps, and the latter turn out to be the most relevant physically.

Specifically, at $c_{\min}$, bifurcate from linear sinusoidal waves of wavenumber $k_{\min}$ two branches of plane solitary waves, one of elevation and the other of depression, which propagate with speed less than $c_{\min}$. In the small-amplitude limit slightly below $c_{\min}$, both types of solitary waves behave as modulated wavepackets, with carrier wavenumber $k_{\min}$ (Akylas 1993; Longuet-Higgins 1993), and at finite steepness they transform into isolated troughs (Longuet-Higgins 1989; Vanden-Broeck & Dias 1992). However, only the depression branch is stable to longitudinal perturbations (Calvo & Akylas 2002), and these solitary waves turn out to be unstable, too, in the presence of transverse perturbations (Kim & Akylas 2007).

The minimum gravity–capillary phase speed, $c_{\min}$, is also the bifurcation point of elevation and depression lumps propagating at speeds less than $c_{\min}$ (Kim & Akylas 2005; Parau, Vanden-Broeck & Cooker 2005). These fully localized steady solutions share several common features with their two-dimensional counterparts. Lump profiles, in particular, are relatively elongated in the transverse direction and resemble qualitatively those of solitary waves along the propagation direction. In regard to their stability properties, however, lumps behave very differently from plane solitary waves: while both lump-solution branches are unstable in the small-amplitude limit,

lumps of depression become stable at finite steepness (see Chapter 2). This suggests that, if viscous dissipation is somehow overcome, steep depression gravity–capillary lumps are likely to be observable. In fact, there is numerical evidence from an undamped model equation that the transverse instability of depression solitary waves indeed results in the formation of finite-amplitude depression lumps (Kim & Akylas 2007).

In contrast to the progress made in the theory of gravity–capillary solitary waves on deep water, there have been only a few related experimental studies. In laboratory-scale wind-wave experiments, Zhang (1995) observed isolated features with sharp curvatures in slope images of the water surface. The features were relatively elongated in one direction, resembling, at least qualitatively, calculated shapes of lumps. Measurements of the profiles across the narrow dimension of these features showed reasonable agreement with computed profiles of plane solitary waves in Longuet-Higgins (1989). In a later laboratory experiment, Longuet-Higgins & Zhang (1997) used a 2-D slit to create a vertically oriented air jet that impinged on the water surface in a recirculating water channel. The plane of the jet was normal to the flow direction and a small amount of chalk powder was used to make the free surface visible. When the free stream water velocity was below $c_{\min}$, a localized wave formed directly beneath the impinging jet. The shape of the free surface showed good agreement with computed plane solitary gravity–capillary waves (Longuet-Higgins 1989), but the wave pattern was not completely steady owing to lateral instabilities, particularly at lower speeds.

The present chapter deals with theoretical and computational investigation of gravity–capillary lumps, generated by a localized pressure source moving over deep water at speeds below $c_{\min}$. A relevant companion experiment was carried out by Dr. Diorio and Professor Duncan at University of Maryland. Similarly to c_0 in shallow water, $c_{\min}$ is a critical forcing speed at which the linear invisicd response becomes singular (Raphaël & de Gennes 1996), and nonlinear effects are expected to come into play as this resonance is approached. In earlier work, assuming potential flow, Parau *et al.* (2005) computed the steady-state wave pattern induced by a localized pressure disturbance moving on the free surface of deep water; as $c_{\min}$ is approached

from below, the response, rather than blowing up as predicted by linear theory, turns around at a certain critical speed less than $c_{\min}$, forming a limit point, and then follows a finite-amplitude solution branch corresponding to essentially free lumps of depression. Calvo & Akylas (2002) examined the stability of this steady-state forced response and found that only the small-amplitude (Rayleigh's) solution branch is stable, suggesting that this state would be realizable for forcing speeds below the limit point. What happens for forcing speeds above the critical speed defined by the limit point, and the possible role of lumps, are open questions that will be addressed in the present investigation.

A related issue is the role of viscous dissipation, that is known to be significant for waves in the gravity–capillary range (Lamb 1993, §348). In their steady-state computations, Parau, Vanden-Broeck & Cooker (2007) introduced a small damping term in the dynamic free-surface condition merely as a device for imposing the radiation condition. We find that, as the forcing speed is increased towards $c_{\min}$, the response is not always steady; moreover, its precise nature is decided by a delicate balance between nonlinearity, which is controlled by the strength of forcing, and viscous dissipation.

4.2 Companion experiment (by J. D. Diorio and J. H. Duncan at University of Maryland)

The companion experiments were carried out in a water tank 7.3 m long and 76 cm wide with water depth of approximately 60 cm (figure 4-1). The tank has glass walls and bottom for optical access. The surface tension was measured *in situ* with a Wilhelmy plate and remained at $\sigma = 73$ dyne/cm throughout the experiments. A pipe with inner diamter $D = 2.5$ mm was mounted vertically to a carriage that rides on top of the tank. The open end of the pipe was positioned 1 cm above the water surface. The carriage was towed at various speeds by a servomotor with a precision of better than 0.3 %. Speed parameter is defined as $\alpha = V/c_{\min}$, where V is the speed of the pipe-carriage assembly and $c_{\min} = 23$ cm/s is the minimum phase speed.

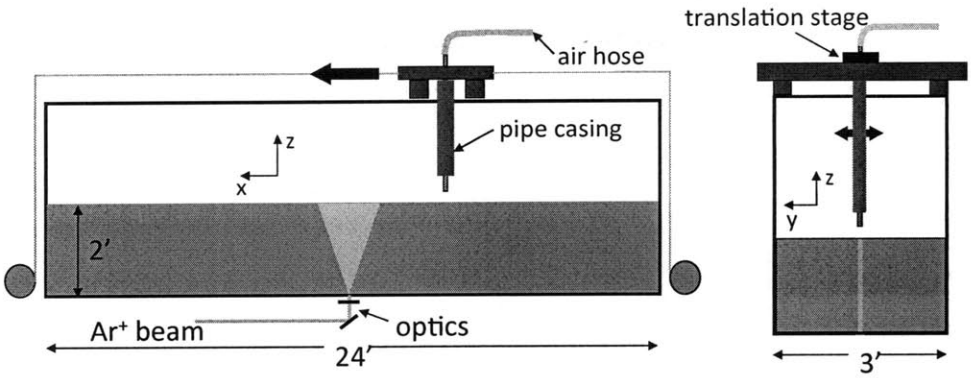

Figure 4-1: Schematic of the experimental setup. A small tube (2.5 mm ID) is mounted in a vibration reducing casing and attached to a movable carriage. A pressurized air line forces air through the tube to generate a small depression on the water surface. A high-speed camera (not shown) images the water surface deformation pattern from the side. The tube is towed in the x (streamwise) direction, and is mounted on a translational stage so it can be displaced in the y (cross-stream) direction. (reproduced under the kind permission of Dr. James Diorio and Professor James Duncan at University of Maryland)

A pressure disturbance is made on the water surface by connecting a pressurized air line to the 2.5 mm pipe. The air flow rate was controlled with a flow metering valve and the nondimensional forcing parameter is defined as $F = h_0/D$, where h_0 is the depth of the depression created by the air forcing when the carriage is stationary. The resulting wave pattern was measured using a high-speed camera combined with a shadowgraph technique.

4.2.1 State I and state II

Figure 4-2 shows the patterns that form as the pipe is towed at various speeds. The pictures were taken with the high-speed camera viewing the water surface from above. The images were backlit using a white light source to creat a contrast; the dark area represents downward sloping face where the light is blocked and the bright area is ridge or crest that are well illuminated. Each photo is from a separate experiment, and the forcing is moving from right to left. At low speeds, there is a symmetric circular depression located directly beneath the air jet (figure 4-2a). We call this

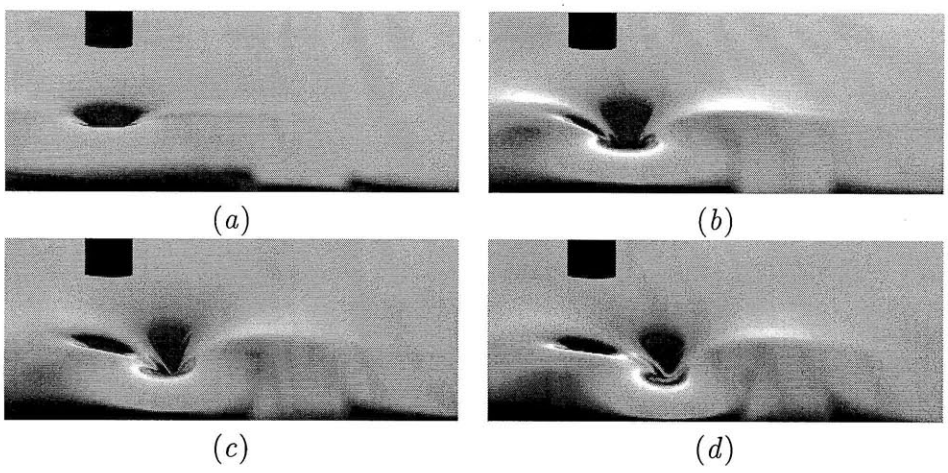

Figure 4-2: Images of the wave pattern taken from above the water surface with the high-speed camera. The forcing parameter is approximately $F = 0.43$. The pressure forcing (and the pipe) are moving from right to left. (a) $\alpha = 0.905$, (b) $\alpha = 0.927$, (c) $\alpha = 0.948$, (d) $\alpha = 0.970$. For scale, note that the outside diameter of the pipe is approximately 3.2 mm. (reproduced under the kind permission of Dr. James Diorio and Professor James Duncan at University of Maryland)

configuration state I. As the speed is increased, the response becomes asymmetric and a stronger depression forms behind the air jet (figure 4-2*b*). This trailing disturbance is longer in the cross-stream than the streamwise direction and is qualitatively similar to a depression gravity–capillary lump of finite steepness; as the speed is increased further, the disturbance moves farther behind the jet (figures 4-2(*b*–*d*)). We call this asymmetric pattern state II. Figure 4-3 shows the maximum depth of the pattern $h_{\min}$, normalized by h_0, versus α when $F = 0.43$. Each point in figure 4-3 comes from a different experimental run. For small values of α, the response is essentially linear, as in figure 4-2*a*. However, at a critical value of the speed parameter, $\alpha_c \approx 0.9$, there is a distinct jump in amplitude which coincides with the transition from the linear, localized, symmetric response (state I) to the nonlinear, extended, asymmetric response (state II). In the vicinity of this transition speed, the response exhibits time-dependent behavior, oscillating between state I and II, but the wave pattern appears to become steady for $\alpha > \alpha_c$.

The effects of F, i.e., the level of surface pressure induced by the air jet, on the surface deformation pattern were also investigated. Some aspects of these effects

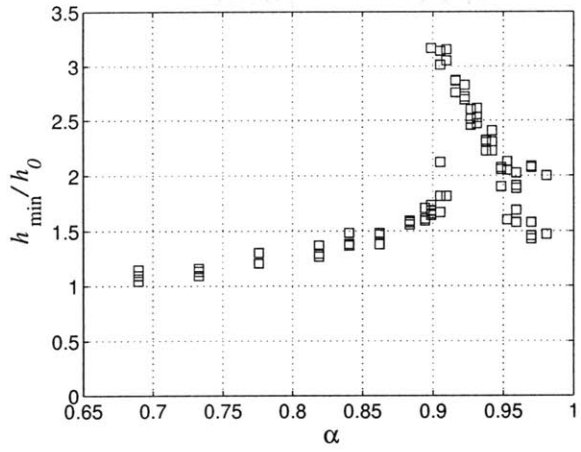

Figure 4-3: Normalized maximum depth, $h_{\min}/h_0$ versus α for $F = 0.43$. Each data point is taken from a different experiment. (reproduced under the kind permission of Dr. James Diorio and Professor James Duncan at University of Maryland)

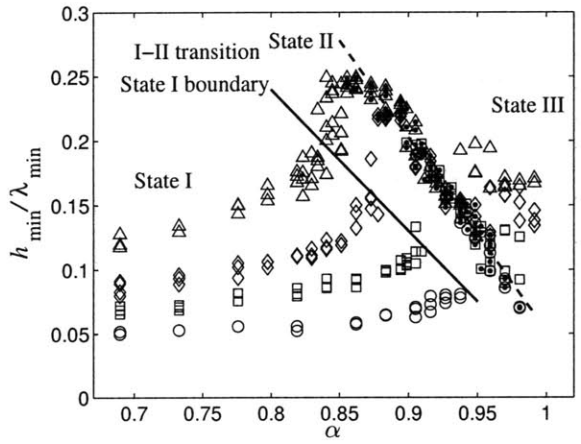

Figure 4-4: Normalized maximum depth of the wave pattern, $h_{\min}/\lambda_{\min}$, versus the speed parameter α. Data taken with four different values of F are shown: $\circ$ $F = 0.30$, $\square$ $F = 0.43$, $\Diamond$ $F = 0.51$, and $\triangle$ $F = 0.69$. Note that all the data fall on a common line in state II (each of these data points is filled with a black dot in the center), independent of the value of F. The straight dashed line, $h_{\min}/\lambda_{\min} = -1.58\alpha + 1.64$, is a least squares fit to the points considered to be in state II. Data points above this line at high values of α are in state III. (reproduced under the kind permission of Dr. James Diorio & Professor James Duncan at University of Maryland)

are shown graphically in the plot of $h_{\min}/\lambda_{\min}$ versus α (where $\lambda_{\min} = 2\pi(\sigma/g\rho)^{1/2}$ is the gravity-capillary wavelength at the minimum phase speed $c_{\min}$) in figure 4-4. Data is presented for all four values of F: 0.30, 0.43, 0.51 and 0.69. Qualitatively, regardless of the value of F, the surface response and the general shape of the curves of $h_{\min}/\lambda_{\min}$ versus α resemble the case discussed above, which is also shown in figure 4-4. However, the details of the $h_{\min}/\lambda_{\min}$ versus α curves show considerable variation from one value of F to another. As can be seen from the figure, the value of α_c and the jump in $h_{\min}/\lambda_{\min}$ at this α decrease with increasing F, while the jump zone occurs over a wider range of α. Also, the value of α where the state II response begins decreases with increasing F. However, one of the most significant features of the plot is that the state-II data points for all four values of F fall on a single curve. The dashed line in the plot is a least-squares fit of a straight line to the state-II data and is given by $h_{\min}/\lambda_{\min} = -1.58\alpha + 1.64$. Similarly, a one-to-one relationship between the depth of the depression and its phase speed is found in the theory and calculations of freely propagating gravity-capillary solitary waves in deep water.

4.2.2 State III and supercritical state

As the towing speed approaches $c_{\min}$, the trailing disturbance completely detaches from the forcing, leading to the formation of a time-dependent V shape as in figure 4-5. We refer to this pattern as state III. The wave pattern in state III has a well-defined cycle. Figure 4-5 shows images of the water surface as the wave passes through one of these cycles. Initially the wave has V shape as shown in figure 4-5*a*. The pattern then stretches out as two disturbances are shed from the tips of the V (figure 4-5*b* and 4-5*c*) producing a more localized, linear response (figure 4-5*d*). The nonlinear response quickly grows again and the V-shaped pattern is observed once more (figure 4-5*e* and 4-5*f*). Finally, as the towing speed exceeds $c_{\min}$, the classic wave radiation "wedge" is formed, with waves both in front of and behind the pressure forcing (figure 4-6).

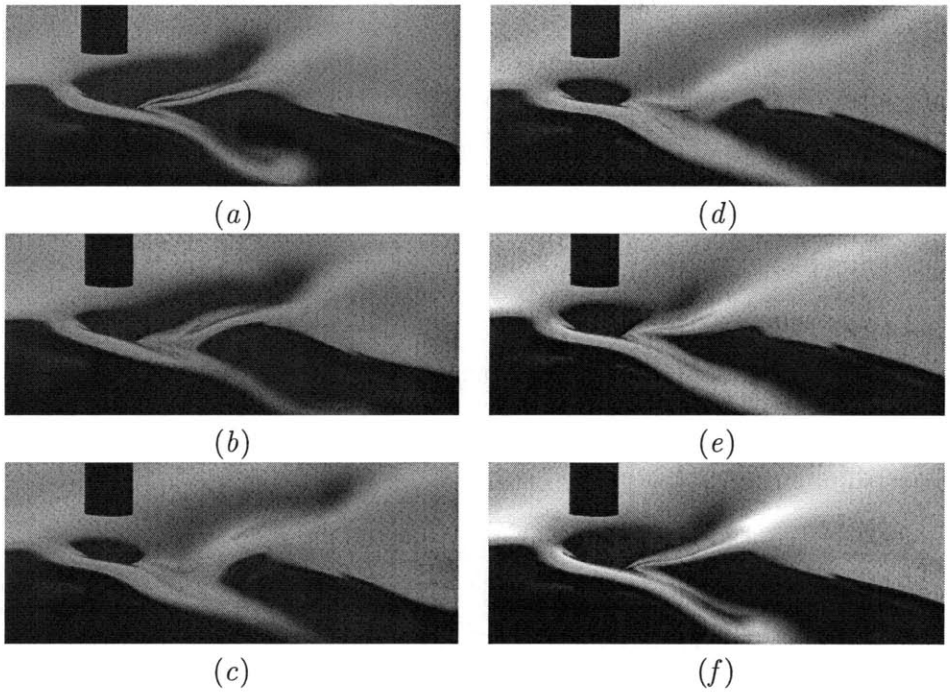

Figure 4-5: Sequence of images showing the "shedding" oscillation of the wave pattern in state III from above the surface for $F = 0.43$ and $\alpha = 0.981$. The images are separated by 0.36 s in time. (reproduced under the kind permission of Dr. James Diorio and Professor James Duncan at University of Maryland)

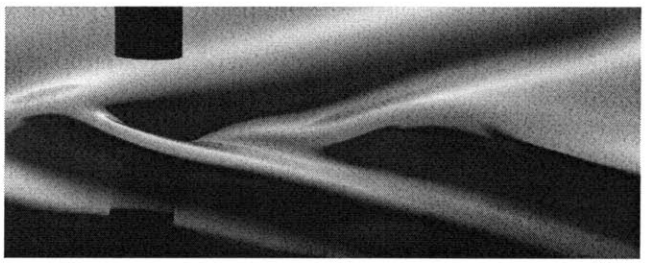

Figure 4-6: Images of the wave pattern taken from above the water surface with the high-speed camera. The forcing parameter is approximately $F = 0.43$. The pressure forcing (and the pipe) are moving from right to left. $\alpha = 0.981$. (reproduced under the kind permission of Dr. James Diorio and Professor James Duncan at University of Maryland)

4.3 Model formulation

We recall that, according to linear potential-flow theory, $c_{\min}$ is a resonant forcing speed, where the response grows unbounded in time, suggesting that nonlinear and viscous effects would likely become important near this critical condition. Moreover, ignoring viscous damping, $c_{\min}$ is the bifurcation point of fully localized solitary waves, or lumps, that may also play a significant role in the resonant forced response.

In the previous sections, laboratory experiments conducted in a tank using as forcing a circular pressure distribution, created by a small tube blowing air onto the water surface are summarized. Now, this section is concerned with an approximate theoretical model, that is used to explain various aspects of the observed responses near critical conditions.

The experimental observations summarized in the previous sections suggest that the wave response to a localized pressure source moving with speed near $c_{\min}$ is controlled by dispersive, nonlinear, three-dimensional and transient effects; also, given that the waves of interest are in the gravity–capillary range, viscous dissipation is expected to play an important part. Moreover, as the response features lumps that are fairly steep, nonlinearity cannot be assumed weak.

Rather than the full unsteady, nonlinear, viscous water-wave problem in three dimensions, the ensuing analysis is based on a simple model equation. Even though it is not obtained from the exact governing equations via a systematic approximation procedure, this equation combines the main effects controlling the response and captures the essential features of the observations. Furthermore, the proposed model adds to the physical understanding of the response by bringing out the delicate interplay between dispersive, nonlinear and viscous effects that takes place near $c_{\min}$. A similar ad-hoc approach is taken in Whitham (1974, §13.14) in an attempt to study water-wave breaking, a phenomenon also not amenable to weakly nonlinear treatment.

We now present the various terms in the model equation. The starting point is the dispersion relation of potential-flow theory for linear sinusoidal gravity–capillary

waves of frequency ω and wavenumber k on deep water,

$$\omega^2 = \tfrac{1}{2}k(1+k^2), \tag{4.1}$$

written in dimensionless form, normalizing to 1 the minimum of the phase speed, $c(k) = \omega/k$, and the corresponding wavenumber $k_{\min}$. On kinematic grounds, at steady state, a locally confined source moving with dimensionless speed α would excite waves that satisfy

$$\alpha \cos\phi = c(|\mathbf{k}|), \tag{4.2}$$

ϕ being the inclination of the wavevector $\mathbf{k}$ to the line of motion of the source (Whitham 1974, §12.4). In the case of interest, where the source speed is close to the minimum phase speed, $\alpha \approx 1$, the kinematic constraint (4.2) requires that $|\mathbf{k}| \approx 1$ and $\phi \ll 1$. Accordingly, a forcing moving along x, say, with near-critical speed would generate waves with $\mathbf{k} = (k, l)$ close to $\mathbf{k}_{\min} = (1, 0)$. This suggests approximating the dispersion relation (4.1) in the neighbourhood of the phase speed minimum; for a left-going source as in the experiment, in particular, expanding (4.1) to second order around $\mathbf{k}_{\min}$ yields

$$\omega = -\tfrac{1}{4}\mathrm{sgn}(k)(1 + 2\,|k| + k^2 + 2l^2). \tag{4.3}$$

To account for viscous dissipation, we shall modify (4.3) by adding an imaginary part representing the wave decay rate due to viscous damping:

$$\omega = -\mathrm{i}\tilde{\nu}\,|\mathbf{k}|^2 - \tfrac{1}{4}\mathrm{sgn}(k)(1 + 2\,|k| + k^2 + 2l^2), \tag{4.4}$$

$\tilde{\nu}$ being a constant. This choice is consistent with the classic result obtained by Lamb (1993, §348) for the viscous decay rate of linear sinusoidal waves, where $\tilde{\nu}$ turns out to be equal to $\tilde{\nu}_0 = \nu(4g)^{1/4}(\rho/\sigma)^{3/4}$, ν being the kinematic viscosity. (In cgs units, $\nu = 0.01$, $g = 981$, $\rho = 1$ and $\sigma = 73$, so $\tilde{\nu}_0 = 0.003$.) More recently, Longuet-Higgins (1997) examined viscous dissipation in deep-water gravity–capillary solitary waves. The expression for the decay rate in (4.4) turns out to be also valid for small-amplitude solitary waves, which resemble modulated wavepackets (Akylas

1993; Longuet-Higgins 1993); in this instance, however, $\tilde{\nu} = 2\tilde{\nu}_0$, due to the spreading out of the wave envelope as the amplitude decreases. In the other extreme, steep depression solitary waves, owing to the sharply increased curvature in the wave troughs, experience far more rapid decay than their weakly nonlinear counterparts. Here, (4.4) will be assumed to hold in general, irrespective of the wave steepness, treating $\tilde{\nu}$ as a parameter that controls the strength of viscous damping.

Based on (4.4), making use of

$$\omega \leftrightarrow \mathrm{i}\frac{\partial}{\partial t}, \quad (k,l) \leftrightarrow -\mathrm{i}(\frac{\partial}{\partial x}, \frac{\partial}{\partial y}), \quad \mathrm{sgn}(k) \leftrightarrow \mathrm{i}\mathcal{H}, \tag{4.5}$$

where $\mathcal{H}\{f\} = \mathcal{F}^{-1}\{-\mathrm{isgn}(k)\mathcal{F}\{f\}\}$ stands for the Hilbert transform, with

$$\mathcal{F}\{f\} = \frac{1}{2\pi}\int_{-\infty}^{\infty} f(x)e^{-\mathrm{i}kx}\mathrm{d}x \tag{4.6}$$

being the Fourier transform, it is straightforward to write down the associated linear differential equation that combines dispersive effects near $c_{\min}$ with viscous damping; adding the effect of forcing due to a pressure source $Ap(\xi, y)$ moving from right to left along x with speed α, the following forced equation for the free-surface elevation $\eta(\xi, y, t)$ is obtained:

$$\eta_t - \tilde{\nu}(\eta_{\xi\xi} + \eta_{yy}) + (\alpha - \tfrac{1}{2})\eta_\xi - \tfrac{1}{4}\mathcal{H}\{\eta_{\xi\xi} + 2\eta_{yy} - \eta\} = Ap_\xi, \tag{4.7}$$

where $\xi = x + \alpha t$ and A is a parameter that controls the peak amplitude of the applied forcing.

To complete the model, it remains to account for nonlinearity. In the interest of simplicity, following Akers & Milewski (2009), we add to (4.7) a quadratic nonlinear term of the Korteweg–de Vries (KdV) type:

$$\eta_t - \tilde{\nu}(\eta_{\xi\xi} + \eta_{yy}) + (\alpha - \tfrac{1}{2})\eta_\xi - \beta(\eta^2)_\xi - \tfrac{1}{4}\mathcal{H}\{\eta_{\xi\xi} + 2\eta_{yy} - \eta\} = Ap_\xi, \tag{4.8}$$

where $\beta = \sqrt{11/2}/8$. This choice for β ensures that, in the small-amplitude limit, free

($A = 0$), inviscid ($\tilde{\nu} = 0$) lump solutions of the model equation (4.8) agree, to leading order, with their weakly nonlinear counterparts of the full potential-flow theory of water waves (Kim & Akylas 2005).

Briefly, small-amplitude inviscid lumps are modulated wavepackets with carrier and envelope propagating at the same speed α slightly below the minimum phase speed ($\alpha < 1$). According to the model equation (4.8), for $\tilde{\nu} = A = 0$, these solutions can be expanded close to their bifurcation point $\alpha = 1$ as

$$\eta = \tfrac{1}{2}\epsilon \left\{ S(X,Y)\mathrm{e}^{\mathrm{i}\xi} + \text{c.c.} \right\} + \tfrac{1}{2}\epsilon^2 \left\{ S_2(X,Y)\mathrm{e}^{2\mathrm{i}\xi} + \text{c.c.} \right\} + \cdots , \tag{4.9}$$

where $\alpha = 1 - \epsilon^2$ ($0 < \epsilon \ll 1$) and $(X,Y) = \epsilon(\xi, y)$. Substituting (4.9) into (4.8), the envelope of the primary harmonic is governed by

$$-S + \tfrac{1}{4}(S_{XX} + 2S_{YY}) + \tfrac{11}{32}S^2 S^* = 0, \tag{4.10}$$

the same steady nonlinear Schrödinger (NLS) equation (after allowing for the difference in normalization) as found in Kim & Akylas (2005) for weakly nonlinear lumps on the basis of potential-flow theory.

While the NLS equation (4.10) provides a link to the full water-wave problem only in the weakly nonlinear limit, we shall use equation (4.8) regardless of wave steepness. The predictions of our model, therefore, are expected to be qualitative at best. For instance, figure 4-7 shows plots of maximum depression against wave speed α of free, inviscid lumps, as obtained from numerical solutions of the model equation (4.8) for $A = \tilde{\nu} = 0$ (Akers & Milewski 2009; Appendix A), the full potential-flow theory of water waves (E. Parau, private communication) and the leading-order weakly nonlinear approximation according to expansion (4.9). The model equation, although it is a definite improvement upon the weakly nonlinear theory away from the bifurcation point, overpredicts the peak amplitude of depression lumps of the exact inviscid theory. This discrepancy can be mitigated to some extent by adding to (4.7), rather than merely a quadratic term, a combination of quadratic and cubic nonlinearities, $(\beta_1\eta^2 + \beta_2\eta^3)_\xi$, choosing the coefficients β_1 and β_2 so that both the $O(\epsilon)$ and $O(\epsilon^2)$

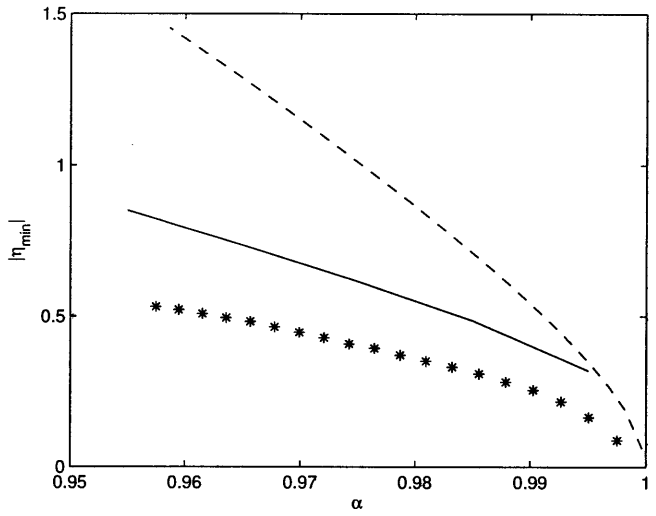

Figure 4-7: Plots of maximum depression, $|\eta_{\min}|$, against wave speed α of free, inviscid lumps of depression. ——: model equation (4.8) with $A = \tilde{\nu} = 0$; -----: leading-order weakly nonlinear approximation; ***: full potential-flow theory (E. Parau, private communication).

terms in expansion (4.9) agree with the full theory (Appendix B). However, the overall gain does not seem worth the added complication, given that the nonlinear nature of viscous damping was ignored earlier, among other assumptions.

4.4 Steady-state responses

Perhaps the most striking nonlinear feature of the wave response as the forcing speed approaches $c_{\min}$, revealed by the experimental observations, is the sudden jump from state I to state II, that occurs at a critical speed $\alpha_c < 1$ depending on the strength of the forcing. State I is locally confined beneath the forcing, similarly to the subcritical response predicted by linear theory (Rayleigh's solution), whereas state II is nonlinear as it features a steep lump downstream of the forcing. In an effort to understand the transition from state I to state II, we shall make a systematic study, based on the model equation (4.8), of steady-state responses as the forcing speed α is increased towards 1, for various values of the forcing amplitude A and damping parameter $\tilde{\nu}$. Throughout this chapter, the forcing disturbance $p(\xi, y)$ in (4.8) will be assumed to

be in the form of a Gaussian centred at $\xi = y = 0$:

$$p(\xi, y) = \exp(-2\xi^2 - 2y^2). \tag{4.11}$$

4.4.1 Shifted lumps

Guided by the nature of state II, we first look for possible subcritical steady-state solutions of (4.8) in the form of a finite-amplitude lump, slightly modified by forcing and damping. To this end, we write

$$\eta = \bar{\eta}(\xi - \theta, y) + \tilde{\eta}(\xi, y). \tag{4.12}$$

Here, $\bar{\eta}$ denotes a free, undamped depression-lump solution of (4.8) with speed $\alpha < 1$,

$$(\alpha - \tfrac{1}{2})\bar{\eta}_\xi - \beta(\bar{\eta}^2)_\xi - \tfrac{1}{4}\mathcal{H}\{\bar{\eta}_{\xi\xi} + 2\bar{\eta}_{yy} - \bar{\eta}\} = 0, \tag{4.13}$$

θ being an as yet undetermined constant shift of the lump profile relative to the forcing, and $\tilde{\eta}$ is a correction term.

Inserting (4.12) into (4.8) and making use of (4.13), it is found that $\tilde{\eta}$ satisfies

$$\begin{aligned}(\alpha - \tfrac{1}{2})\tilde{\eta}_\xi - 2\beta\big(\bar{\eta}(\xi - \theta, y)\tilde{\eta}\big)_\xi - \tfrac{1}{4}\mathcal{H}\{\tilde{\eta}_{\xi\xi} + 2\tilde{\eta}_{yy} - \tilde{\eta}\} \\ = \tilde{\nu}(\bar{\eta}_{\xi\xi} + \bar{\eta}_{yy}) + Ap_\xi + \tilde{\nu}(\tilde{\eta}_{\xi\xi} + \tilde{\eta}_{yy}) + \beta(\tilde{\eta}^2)_\xi.\end{aligned} \tag{4.14}$$

Taking forcing and damping effects to be weak ($A \ll 1, \tilde{\nu} \ll 1$), we put

$$\tilde{\nu} = \mu A, \tag{4.15}$$

μ being a parameter that measures the relative importance of damping, and expand the solution to (4.14) as

$$\tilde{\eta} = A\tilde{\eta}^{(1)} + A^2\tilde{\eta}^{(2)} + \cdots, \tag{4.16}$$

with a similar expansion for the shift θ:

$$\theta = \theta^{(0)} + A\theta^{(1)} + \cdots . \tag{4.17}$$

The same sort of perturbation procedure has also been used in analyzing finite-amplitude steady-solution branches of a forced–damped fifth-order KdV equation (Cho & Akylas 2009; Chapter 3).

Upon substituting (4.16) into (4.14) and using (4.15) and (4.17), it is found that $\tilde{\eta}^{(1)}$ is governed by the forced equation

$$(\alpha - \tfrac{1}{2})\tilde{\eta}^{(1)}_{\xi} - 2\beta\big(\bar{\eta}(\xi - \theta^{(0)}, y)\tilde{\eta}^{(1)}\big)_{\xi} - \tfrac{1}{4}\mathcal{H}\left\{\tilde{\eta}^{(1)}_{\xi\xi} + 2\tilde{\eta}^{(1)}_{yy} - \tilde{\eta}^{(1)}\right\} = R^{(1)}, \tag{4.18}$$

where

$$R^{(1)} = p_{\xi} + \mu(\bar{\eta}_{\xi\xi}(\xi - \theta^{(0)}, y) + \bar{\eta}_{yy}(\xi - \theta^{(0)}, y)). \tag{4.19}$$

The adjoint to the operator on the left side of (4.18) is

$$(\alpha - \tfrac{1}{2})\frac{\partial}{\partial\xi} - 2\beta\bar{\eta}(\xi - \theta^{(0)}, y)\frac{\partial}{\partial\xi} - \tfrac{1}{4}\mathcal{H}\left\{\frac{\partial^2}{\partial\xi^2} + 2\frac{\partial^2}{\partial y^2} - 1\right\}, \tag{4.20}$$

and, in view of (4.13), $\bar{\eta}(\xi - \theta^{(0)}, y)$ is a homogeneous adjoint solution that goes to zero as $\xi \to \pm\infty$, $y \to \pm\infty$. Therefore, appealing to the standard solvability argument, for the forced equation (4.18) to also have a well-behaved solution, the forcing $R^{(1)}$ must satisfy

$$\int_{-\infty}^{\infty}\int_{-\infty}^{\infty} R^{(1)}\bar{\eta}(\xi - \theta^{(0)}, y)\mathrm{d}\xi\mathrm{d}y = 0. \tag{4.21}$$

Making use of (4.19), the solvability condition (4.21) takes the form

$$\mu\int_{-\infty}^{\infty}\int_{-\infty}^{\infty}(\bar{\eta}_{\xi}^2 + \bar{\eta}_{y}^2)\mathrm{d}\xi\mathrm{d}y = -\int_{-\infty}^{\infty}\int_{-\infty}^{\infty} p(\xi, y)\bar{\eta}_{\xi}(\xi - \theta^{(0)}, y)\mathrm{d}\xi\mathrm{d}y; \tag{4.22}$$

this furnishes an equation for determining the shift $\theta^{(0)}$, depending on the forcing speed α and the parameter μ.

Note that $\theta^{(0)}$ appears only on the right-hand side of (4.22), while μ solely mul-

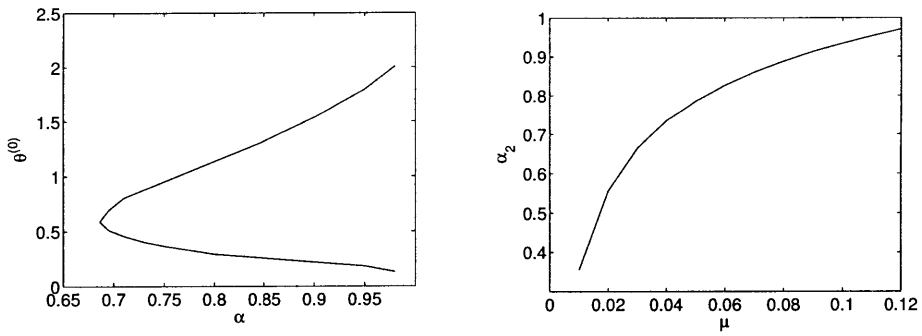

Figure 4-8: Predictions of solvability condition (4.22) regarding the lump accompanying state II. (a) Downstream shift $\theta^{(0)}$ of lump relative to the forcing profile versus forcing speed α, for $\mu = 0.033$; the parameter μ defined in (4.15) measures the importance of damping relative to forcing. (b) Limit point $\alpha = \alpha_2$ below which shifted-lump solution is not possible, as a function of μ.

tiplies the left side. For $\mu = 0$, in particular, since $p(\xi, y)$ is even in ξ according to (4.11), $\theta^{(0)} = 0$ satisfies (4.22) regardless of α. As expected, in the absence of damping, the proposed response (4.12) is symmetric relative to the forcing and tends to the free-lump solution as α becomes more subcritical. On the other hand, for $\mu > 0$, the solvability condition (4.22) can be satisfied for two non-zero values of $\theta^{(0)}$ when α exceeds a certain threshold value, α_2, depending on μ, but no solution is possible if $\alpha < \alpha_2$, as illustrated in figure 4-8(a) for the case $\mu = 0.033$. Accordingly, damping causes finite-amplitude steady-state solution branches to eventually turn around as α is decreased, and the turning point $\alpha = \alpha_2$ moves further away from $\alpha = 1$ when μ is decreased (figure 4-8b). Moreover, since $\mu = \tilde{\nu}/A$, increasing the forcing amplitude A has the same effect as reducing the damping parameter $\tilde{\nu}$.

It is interesting that the values of $\theta^{(0)}$ for $\mu = 0.033$ displayed in figure 4-8(a) are positive, and this turns out to be generally the case in the range $0.01 \leq \mu \leq 0.1$ we examined. The lump profile in (4.12) is thus shifted in the downstream direction relative to the applied forcing, consistent with state II. In fact, as discussed below, tracing of finite-amplitude steady-state solution branches via numerical continuation reveals that state II is associated with the larger of the two possible values of $\theta^{(0)}$ for $\alpha > \alpha_2$.

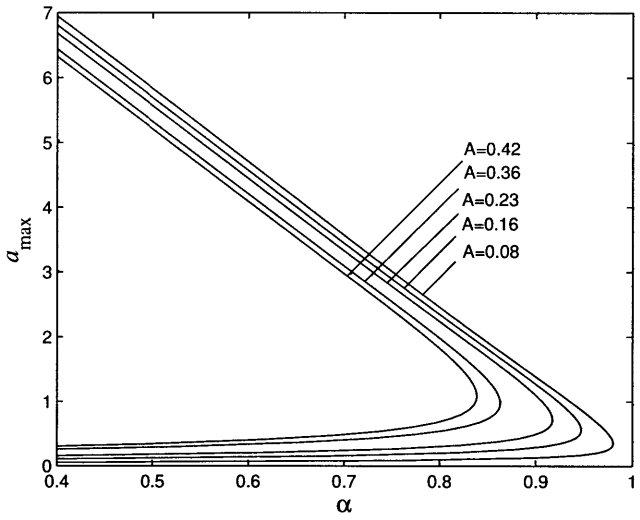

Figure 4-9: Inviscid ($\tilde{\nu} = 0$) steady-state response diagrams of maximum depression, $|\eta_{\min}|$, versus forcing speed α for five different forcing amplitudes A.

4.4.2 Numerical continuation

For highly subcritical forcing speed α and small forcing amplitude A, the solution to the model equation (4.8) is expected to reach the linear subcritical steady state (Rayleigh's solution), that is locally confined in the vicinity of the forcing, similarly to state I. Using numerical continuation, we shall now follow this small-amplitude steady-state solution branch as α is increased towards 1, for different values of A and $\tilde{\nu}$, in order to make connection with the finite-amplitude states found by perturbation theory in §4.4.1.

The steady version of equation (4.8) was discretized using fourth-order centred finite differences, and the Hilbert transform was computed using the discrete Hilbert transform (Kak 1970). Exploiting symmetry, only $y \geq 0$ was considered, and the edges of the computational domain, ($\xi_{-\infty} < \xi < \xi_{+\infty}, 0 \leq y < y_{+\infty}$), were placed far enough so as to have negligible effect on the overall response. The resulting nonlinear equation system was solved by Newton's method, combined with pseudo-arclength continuation (Appendix C). The results reported here were obtained using 256 grid points along ξ and 64 grid points along y with $\xi_{+\infty} = -\xi_{-\infty} = y_{+\infty} = 18.85$.

We first consider the inviscid limit, $\tilde{\nu} = 0$, where the subcritical response is symmetric relative to the forcing. As α is increased, Rayleigh's solution branch turns around at a limit point before reaching $\alpha = 1$ and then follows asymptotically the finite-amplitude solution branch corresponding to free, inviscid lumps. This result is consistent with the perturbation analysis for $\mu = 0$ as well as the full potential-flow computations of Parau *et al.* (2005). The location of the limit point, $\alpha = \alpha_c$, is quite sensitive to the forcing amplitude A, α_c moving closer to $\alpha = 1$ as A is decreased (figure 4-9). For the choice $A = 0.23$, in particular, it turns out that $\alpha_c = 0.92$, which matches approximately the critical speed where transition from state I to state II was observed experimentally for the experimental forcing amplitude $F = 0.43$.

Next, we turn to the role of dissipation ($\tilde{\nu} > 0$). Figure 4-10 summarizes the results of numerical continuation in α of the small-amplitude subcritical solution branch, for $A = 0.23$ and four different values of $\tilde{\nu}$, expressed in terms of $\tilde{\nu}_0 = 0.003$, the value of $\tilde{\nu}$ pertaining to linear waves (Lamb 1993, §348). Compared to the invisicd response diagram (figure 4-9), for the two lower values of $\tilde{\nu} = \tilde{\nu}_0$, $2\tilde{\nu}_0$ (figure 4-10*a*, *b*), the effect of dissipation becomes evident only after passing the turning point at $\alpha_c = 0.92$: as α is decreased past α_c, the response initially stays close to the inviscid one, but later a second turning point, $\alpha = \alpha_2$, is encountered where the solution reverses course again, heading back towards $\alpha = 1$ along a neighbouring path. A qualitatively similar behaviour is also found for the two larger values of $\tilde{\nu} = 6\tilde{\nu}_0$, $8\tilde{\nu}_0$; stronger dissipation, though, affects the entire response diagram, including the critical speed at which the first turning point occurs (figure 4-10*c*, *d*).

The presence of a second turning point, due to dissipation, in the response diagrams shown in figure 4-10 confirms the predictions of the perturbation theory (figure 4-8), and the analytical estimates for α_2 based on (4.22) are in reasonable agreement with the values obtained from numerical continuation (see table 4-1). In line with the perturbation analysis, both before and after turning around at α_2, the numerically computed responses feature a finite-amplitude depression lump shifted downstream relative to the forcing; the downstream shift becomes more noticeable after turning around at α_2 and keeps increasing while the lump steepness decreases, as α moves

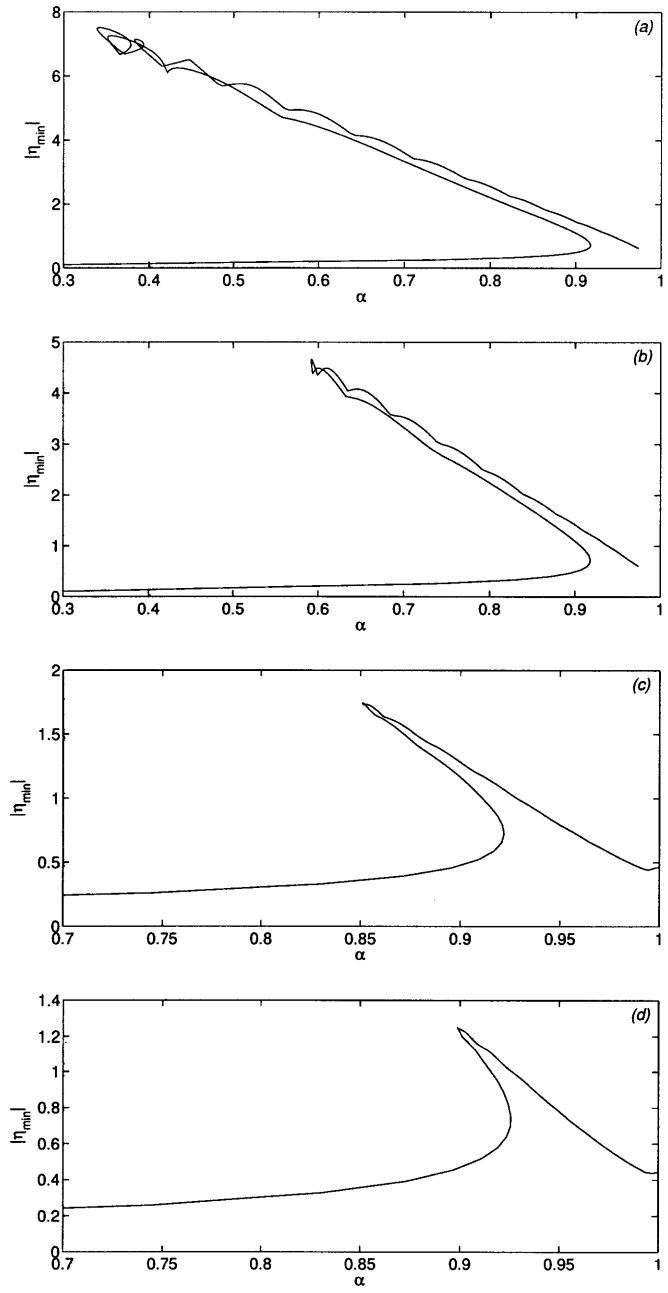

Figure 4-10: Steady-state response diagrams of maximum depression, $|\eta_{\min}|$, versus forcing speed α, for forcing amplitude $A = 0.23$ and four different damping parameters $\tilde{\nu}$. (a) $\tilde{\nu} = \tilde{\nu}_0$; (b) $\tilde{\nu} = 2\tilde{\nu}_0$; (c) $\tilde{\nu} = 6\tilde{\nu}_0$; (d) $\tilde{\nu} = 8\tilde{\nu}_0$; $\tilde{\nu}_0 = \nu(4g)^{1/4}(\rho/\sigma)^{3/4} = 0.003$ is the value of $\tilde{\nu}$ pertaining to linear waves (Lamb 1993, §348)

		α_2	
$\tilde{\nu}$	μ	Numerical	Analytical
$\tilde{\nu}_0$	0.014	0.34	0.44
$2\tilde{\nu}_0$	0.028	0.59	0.64
$6\tilde{\nu}_0$	0.083	0.85	0.89
$8\tilde{\nu}_0$	0.110	0.90	0.95

Table 4.1: Second limit point $\alpha = \alpha_2$ for forcing amplitude $A = 0.23$ and four different values of the damping parameter $\tilde{\nu}$, where $\tilde{\nu}_0 = \nu(4g)^{1/4}(\rho/\sigma)^{3/4} = 0.003$ is the value of $\tilde{\nu}$ pertaining to linear waves (Lamb 1993, §348). The analytical estimates for α_2 were deduced from the solvability condition (4.22), using $\mu = \tilde{\nu}/A$; the numerical values of α_2 were obtained via continuation in forcing speed α of the small-amplitude steady-state subcritical response.

further away from α_2. Figure 4-11 shows representative wave profiles at four different speeds along the response curve for $A = 0.23$ and $\tilde{\nu} = 2\tilde{\nu}_0$ (figure 4-10*b*). We recall that, for this A, the first turning point, $\alpha_c = 0.92$, according to the model, is close to the critical speed at which the jump from state I to state II was observed experimentally for forcing amplitude $F = 0.43$; the speeds of the profiles displayed in figure 4-11 match those of the four experimentally observed profiles in figure 4-2(*a*–*d*), that illustrate the transition of the response from state I (figure 4-2*a*) to state II (figure 4-2(*b*–*d*)) for $F = 0.43$. The computed steady-state responses (figure 4-11) exhibit qualitatively similar behaviour to the observed disturbances. As α is increased past α_c, in particular, the lump accompanying state II is shifted further downstream, becoming less steep and more spread out in the spanwise direction, consistent with the observations.

Finally, for $\tilde{\nu} = \tilde{\nu}_0, 2\tilde{\nu}_0$, where dissipation is relatively low, carrying on the continuation beyond the stage shown in figure 4-10(*a*, *b*) reveals a rather intricate behaviour, with the emergence of steady states comprising multiple lumps. Figure 4-12 shows the detailed path followed by the solution branch for the case $\tilde{\nu} = 2\tilde{\nu}_0$, and figure 4-13 displays the wave profiles corresponding to four locations along the way, marked *a*–*d* in figure 4-12. Note that a third turning point occurs at $\alpha_3 = 0.974$; just prior to reaching there, the response still resembles state II (figure 4-13*a*), but after turning

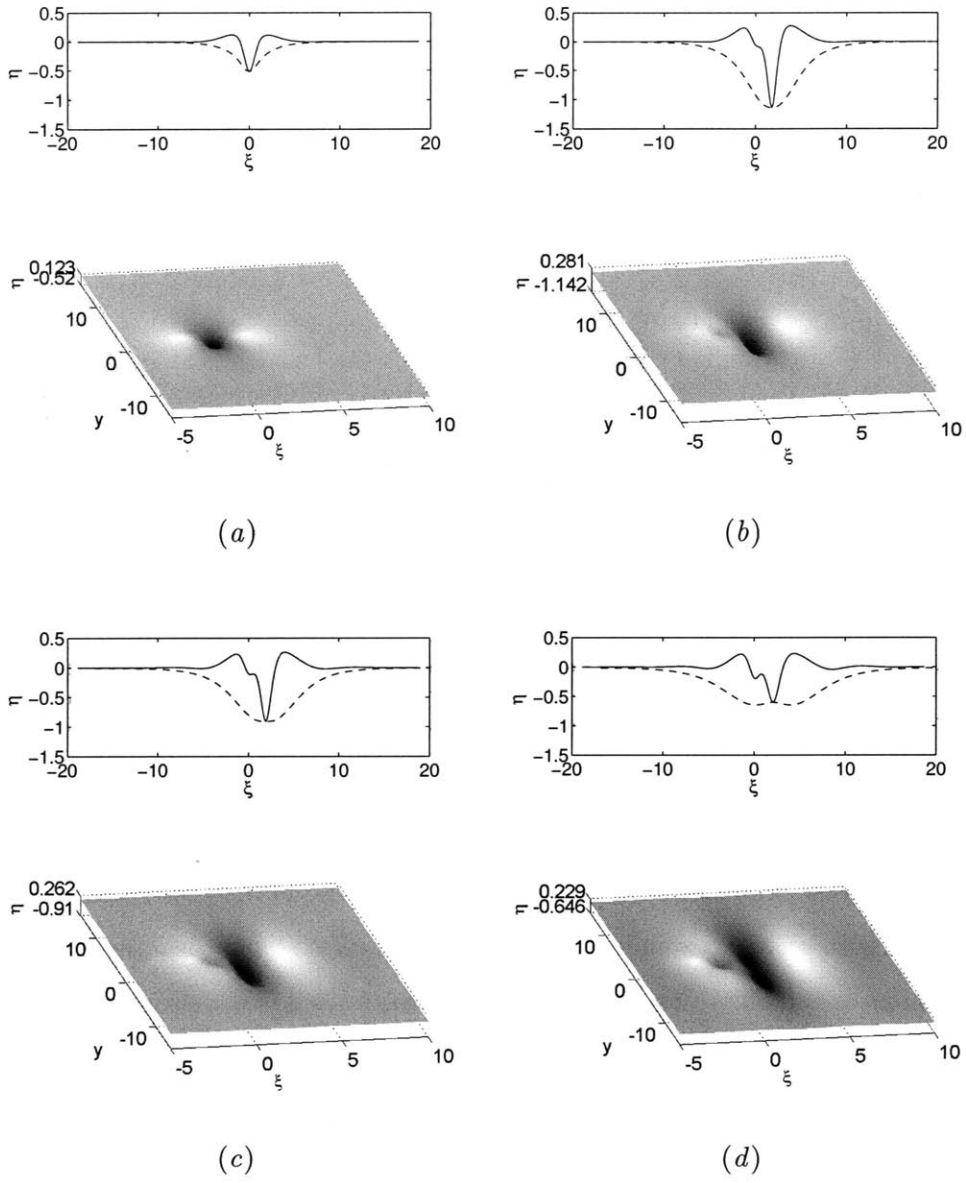

Figure 4-11: Representative steady-state wave profiles at four different forcing speeds α along the response curve shown in figure 4-10(b), for forcing amplitude $A = 0.23$ and damping parameter $\tilde{\nu} = 2\tilde{\nu}_0$, where $\tilde{\nu}_0 = 0.003$. The solid line corresponds to the centreline profile, $\eta(\xi, y = 0)$, and the dashed line to the transverse profile at the station ξ where the maximum depression is found. (a) $\alpha = 0.905$, (b) $\alpha = 0.927$, (c) $\alpha = 0.948$, (d) $\alpha = 0.97$. These speeds match those of the four experimentally observed responses in figure 4-2.

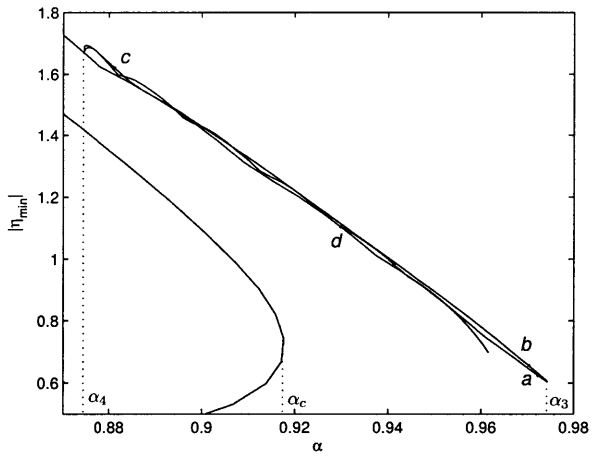

Figure 4-12: Continuation in the forcing speed α past the second limit point at $\alpha = 0.59$ (not shown) of nonlinear solution branch for forcing amplitude $A = 0.23$ and damping parameter $\tilde{\nu} = 2\tilde{\nu}_0$, where $\tilde{\nu}_0 = 0.003$. $|\eta_{\min}|$ stands for the maximum depression of the response. $\alpha_c = 0.918$ is the first limit point, where the small-amplitude state turns around; $\alpha_3 = 0.974$ and $\alpha_4 = 0.875$ denote the third and fourth turning points, respectively. The wave profiles corresponding to the four points marked *a*–*d* along the path followed by the nonlinear solution branch, are plotted in figure 4-13.

around at α_3 a new steady state emerges featuring two lumps downstream of the forcing (figure 4-13*b*). Upon further continuation along the same solution branch, the disturbance beneath the forcing transforms into a third lump (figure 4-13*c*), and the entire pattern is shifted downstream (figure 4-13*d*) after encountering a fourth turning point at $\alpha_4 = 0.875$. This appears to set the stage for the bifurcation of a new state involving more lumps, but will shall not pursue this possibility.

4.5 Transient evolution

The steady-state analysis in §4.4 suggests that the transition from state I to state II is associated with the limit point $\alpha = \alpha_c$, where the response jumps from the small-amplitude state to the nonlinear solution branch that comes close to $\alpha = 1$ after turning around, due to dissipation, at the second limit point, $\alpha = \alpha_2$ (figure 4-10). This scenario presumes that the nonlinear solution branch is stable, which remains

to be established. Also, according to the experimental observations, as the forcing speed is increased past α_c, there is a second transition, from state II, which is steady, to state III, which is unsteady. To address these issues, we shall turn to numerical investigation of transient responses based on the model equation (4.8).

The numerical technique for solving (4.8) used a spectral approximation in space, combined with a predictor–corrector Euler time stepping (Appendix D). The results reported here were obtained using the computational domain ($-37.7 < \xi < 37.7, -31.4 < y < 31.4$) with 512 grid points along ξ, 256 grid points along y and time step $\Delta t = 10^{-3}$.

4.5.1 Stability of state II

Rather than a formal spectral analysis, the stability of state II was explored by direct numerical integration of (4.8), employing as initial condition the steady solution obtained from continuation and letting numerical error act as the perturbation.

We first tested the stability of state II for forcing amplitude $A = 0.23$ and dissipation parameter $\tilde{\nu} = \tilde{\nu}_0, 2\tilde{\nu}_0$. Under these conditions, and forcing speed above α_c, state II is availabe in the finite range $\alpha_c < \alpha < \alpha_3$, $\alpha = \alpha_3$ being the third turning point encountered earlier in the course of the continuation (figure 4-12), with $\alpha_3 = 0.975$ for $\tilde{\nu} = \tilde{\nu}_0$ and $\alpha_3 = 0.974$ for $\tilde{\nu} = 2\tilde{\nu}_0$. Although the steady-state response diagrams corresponding to these two values of $\tilde{\nu}$ (figure 4-10 *a*, *b*) are similar qualitatively, our numerical experiments suggest that state II is unstable for $\tilde{\nu} = \tilde{\nu}_0$, but stable for $\tilde{\nu} = 2\tilde{\nu}_0$, throughout the speed range $\alpha_c < \alpha < \alpha_3$. Figure 4-14 illustrates the totally different stability behaviour of state II for $\tilde{\nu} = \tilde{\nu}_0, 2\tilde{\nu}_0$ when $\alpha = 0.93$. The oscillatory instability seen for $\tilde{\nu} = \tilde{\nu}_0$ is also consistent with the computations reported in Diorio *et al.* (2009). Our earlier study used the model equation (4.8) with $\tilde{\nu} = \tilde{\nu}_0$, and the transient response from rest for $A = 0.21$ and forcing speed α above α_c was found to be periodic in time rather than approaching steady state II.

Based on the present stability computations, when $\tilde{\nu} = \tilde{\nu}_0$, state II turns out to be unstable for $0.08 \leq A \leq 0.36$, corresponding to $0.86 \leq \alpha_c \leq 0.98$, which covers the whole range of forcing amplitudes $0.3 \leq F \leq 0.69$ used in the experiment

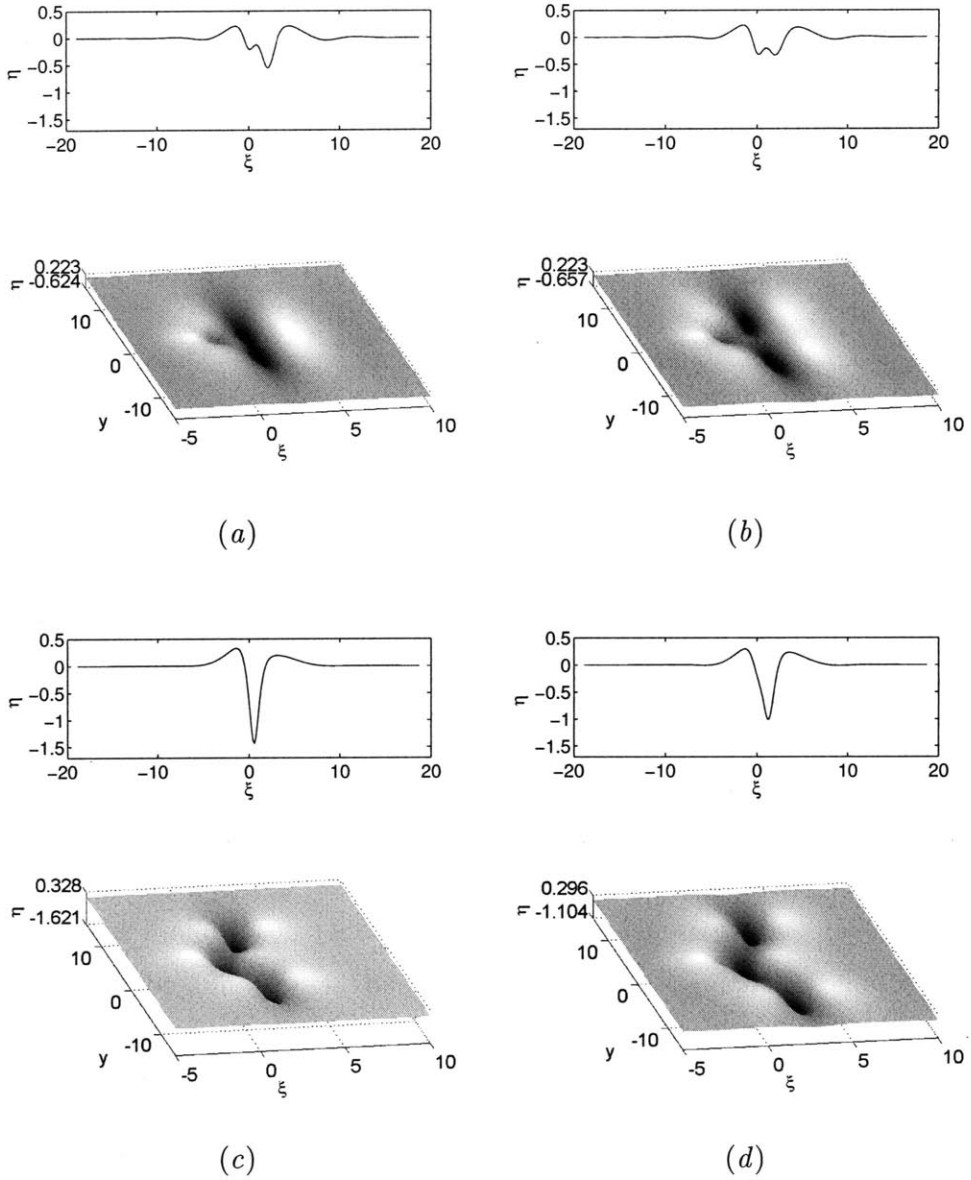

Figure 4-13: Steady-state profiles at the four points marked a–d in figure 4-12 along the path followed by the nonlinear solution branch beyond its second turning point. The one-dimensional plots display the centreline profile $\eta(\xi, y = 0)$. The corresponding forcing speeds are: (a) $\alpha = 0.972$, (b) $\alpha = 0.97$, (c) $\alpha = 0.881$, (d) $\alpha = 0.930$.

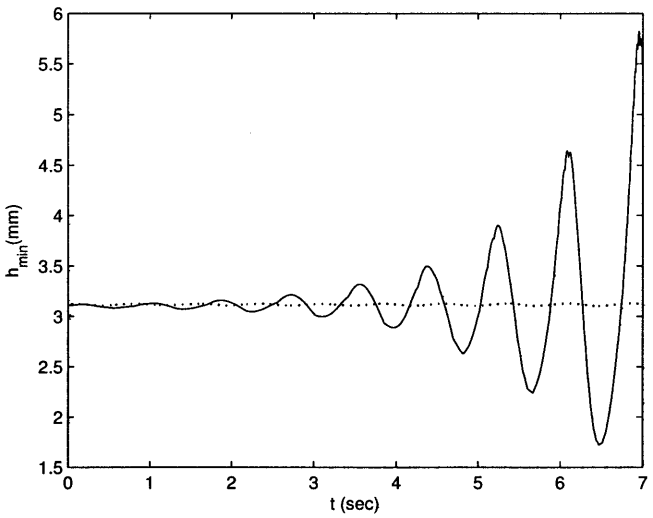

Figure 4-14: Time history of maximum depression, $h_{\min}$ (in mm), as obtained from numerical solution of the model equation (4.8) using as initial condition state II, computed via continuation, for forcing amplitude $A = 0.23$, forcing speed $\alpha = 0.93$ and two different values of the damping parameter $\tilde{\nu}$. (—): $\tilde{\nu} = \tilde{\nu}_0$, $(\cdots)$: $\tilde{\nu} = 2\tilde{\nu}_0$, where $\tilde{\nu}_0 = 0.003$ is the value of $\tilde{\nu}$ pertaining to linear waves.

(figure 4-4). Hence, according to our model, $\tilde{\nu}$ must be greater than $\tilde{\nu}_0$, the value of $\tilde{\nu}$ appropriate for linear waves, in order for state II to be stable, as observed experimentally. This seems reasonable, given that the effect of dissipation in steep gravity–capillary solitary waves is considerably stronger than in linear disturbances (Longuet-Higgins 1997), and one would expect the same to be true for lumps as well. However, as the assumed damping term in (4.8) is linear, it is not possible to account for nonlinear effects in viscous dissipation from first principles. In an attempt to allow for this effect in a rough sense, for the remainder of the chapter, we shall use $\tilde{\nu} = 2.4\tilde{\nu}_0$; this choice implies somewhat stronger viscous dissipation than in weakly nonlinear solitary waves, in which case $\tilde{\nu} = 2\tilde{\nu}_0$ (Longuet-Higgins 1997), and also appears to provide the best overall fit of the model with the observations.

4.5.2 Transition from state I to state II

We next studied the transient response from rest. The model equation (4.8) with $\tilde{\nu} = 2.4\tilde{\nu}_0$ was integrated numerically turning on the forcing impulsively at $t = 0$. Several

runs were made for forcing amplitude $0.08 \leq A \leq 0.36$ and speed $0.7 \leq \alpha \leq 1.03$. As noted above, these conditions cover the entire range of forcing amplitudes and speeds used in the experiment. On the whole, our computations confirm that three distinct subcritical reponses, namely states I, II and III, are possible. Here, we focus on states I and II; state III will be discussed in §4.5.3.

The transient response from rest invariably tends to the small-amplitude steady solution (state I) when the forcing speed $\alpha < \alpha_c$. Upon crossing α_c, however, state I is no longer available and is replaced by state II for $\alpha_c < \alpha < \alpha_3$, where α_3 denotes the third turning point of the finite-amplitude solution branch computed earlier (figure 4-12). Based on numerical experiments (see §4.5.1), for $\tilde{\nu} = 2.4\tilde{\nu}_0$ and $0.08 \leq A \leq 0.36$, state II is stable when $\alpha_c < \alpha < \alpha_3$, and the transient response from rest indeed tends to state II within this range of forcing speeds.

For both state I and state II, the approach to steady state features decaying oscillations, with period of roughly 1 s, as illustrated in figure 4-15 for $A = 0.23$. Similar behaviour was also seen in the experiment, particularly for forcing speeds in the vicinity of α_c. According to our computations, the transition from state I to state II at $\alpha = \alpha_c$ is sharp, the response invariably tending to one of these two states depending on whether $\alpha < \alpha_c$ or $\alpha > \alpha_c$.

As remarked earlier, α_c is quite sensitive to the forcing amplitude A and so is α_3, the upper limit of the speed range $\alpha_c < \alpha < \alpha_3$ in which state II is available. Table 4-2 lists the values of α_c and α_3, obtained from numerical continuation as explained in §4.4.2, for $\tilde{\nu} = 2.4\tilde{\nu}_0$ and the five forcing amplitudes used earlier in the undamped ($\tilde{\nu} = 0$) response diagrams in figure 4-9. While α_c is practically unaffected by the presence of damping, α_3 owes its existence to a delicate balance between forcing and damping; for the weakest of the forcings, $A = 0.08$, in particular, no third turning point, α_3, is found. In this instance, state II is weakly nonlinear and conncets directly with the small-amplitude supercritical response as α is increased past 1.

Figure 4-16 displays the solution branches associated with state I ($\alpha < \alpha_c$) and state II ($\alpha_c < \alpha < \alpha_3$) for four forcing amplitudes A. It is interesting to compare these results to the experimental plots of normalized maximum response depth against

A	α_c	α_3
0.08	0.982	—
0.16	0.948	0.989
0.23	0.918	0.975
0.36	0.864	0.952
0.42	0.839	0.942

Table 4.2: First ($\alpha = \alpha_c$) and third ($\alpha = \alpha_3$) limit points encountered along the continuation in the forcing speed α of the small-amplitude steady-state subcritical response, for damping parameter $\tilde{\nu} = 2.4\tilde{\nu}_0$, where $\tilde{\nu}_0 = 0.003$, and five different forcing amplitudes A.

forcing speed α, shown in figure 4-4, for four experimental forcing amplitudes F. The theoretical forcing amplitudes A have been chosen so that the corresponding values of α_c match roughly the critical speeds at which the response was observed to jump from state I to state II, for the four values of F used in the experiment. It is not surprising, then, that the boundary of state I is well reproduced by the model. More importantly, however, there is also good qualitative agreement with the experiment in regard to the behaviour of state II. Note, in particular, that the theoretical response curves corresponding to state II in figure 4-16 essentially follow the same line for all four values of A, similarly to the experimental data in state II, which collapse on a common line independent of F.

4.5.3 State III

The transition from state II to state III is associated with the third turning point, α_3; state II is not available beyond this speed, and the transient response from rest approaches a periodic state in time, as illustrated in figure 4-17 for $\alpha = 0.981$ when $A = 0.23$. Note that, for this forcing amplitude, $\alpha_3 = 0.975$, which explains the very different time history of the response in figure 4-17 compared to that for $\alpha = 0.97$ in figure 4-15.

State III is characterized by periodic shedding of lump-like disturbances downstream of the forcing. Figure 4-18 displays snapshots of the computed response for $\alpha = 0.981$ and $A = 0.23$ at eight times, separated by 0.36 s, that illustrate a full

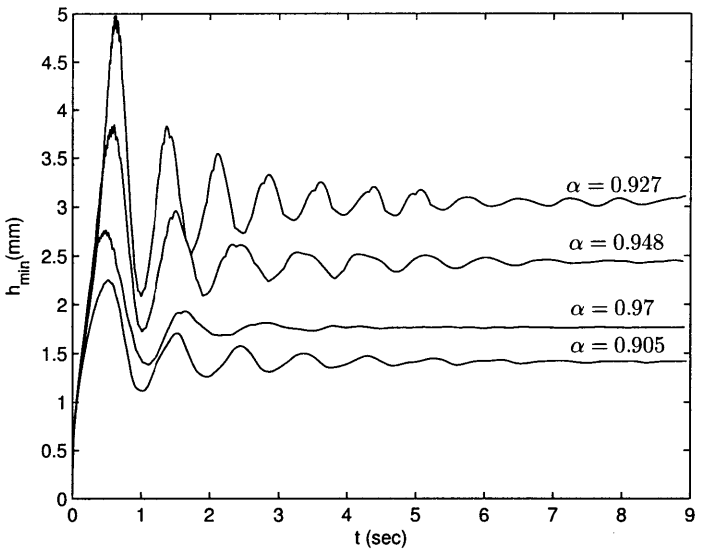

Figure 4-15: Time history of maximum depression, $h_{\min}$ (in mm), associated with transient response starting from rest, for forcing amplitude $A = 0.23$, damping parameter $\tilde{\nu} = 2.4\tilde{\nu}_0$, where $\tilde{\nu}_0 = 0.003$, and four different forcing speeds α. Under these conditions, the response from rest reaches a steady state: state I for $\alpha = 0.905$, but state II for the three higher speeds.

cycle of the shedding process after the periodic state has been reached. At the early stages of the cycle, the pattern has a V shape trailing the forcing (figure 4-18*a*), but soon the tips of the V transform into lumps (figure 4-18*b*, *c*) and the disturbance is reminiscent of the steady states with multiple lumps downstream, computed earlier (figure 4-13*c*, *d*); here, however, the lumps detach from the rest of the disturbance and are quickly damped out (figure 4-18(*d*–*g*)), thus preparing the way for the cycle to start anew (figure 4-18*h*). These results are in good qualitative agreement with the experimental observations regarding state III (figure 4-5). Finally, upon increasing α past the critical value $\alpha = 1$, the response from rest returns to a steady state, as illustrated in figure 4-17 for $\alpha = 1.03$ when $A = 0.23$. This supercritical state is of small-amplitude and has a V shape (figure 4-19), consistent with figure 4-6. The transition from state III to the supercritical state has not been studied in detail.

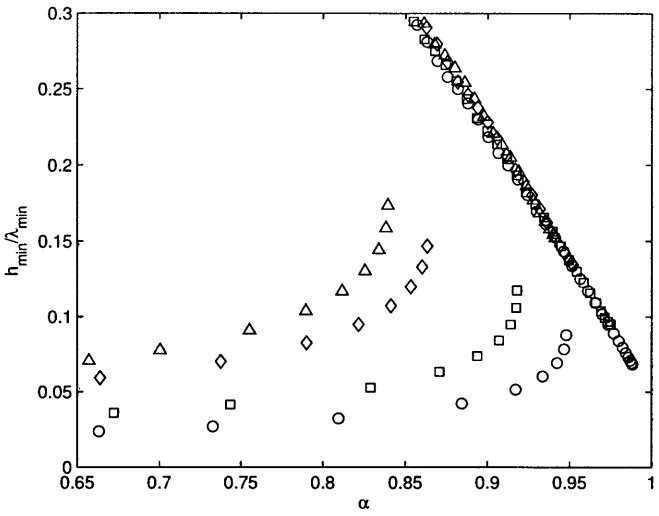

Figure 4-16: Response amplitudes corresponding to state I and state II as the forcing speed α is varied, for damping parameter $\tilde{\nu} = 2.4\tilde{\nu}_0$, where $\tilde{\nu}_0 = 0.003$ and four different forcing amplitudes A. ($\circ$) $A = 0.16$, ($\square$) $A = 0.23$, ($\diamond$) $A = 0.36$, ($\triangle$) $A = 0.42$. As in figure 4-4, $h_{\min}/\lambda_{\min}$ stands for the maximum depression of the response normalized with $\lambda_{\min} = 17.1$ mm, the gravity–capillary wavelength at $c_{\min}$.

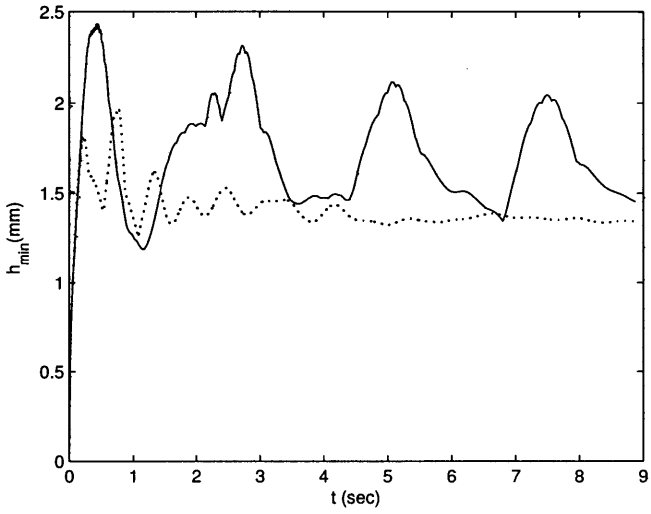

Figure 4-17: Time history of maximum depression, $h_{\min}$ (in mm), associated with transient response starting from rest, for forcing amplitude $A = 0.23$, damping parameter $\tilde{\nu} = 2.4\tilde{\nu}_0$, where $\tilde{\nu}_0 = 0.003$, and two different forcing speeds α. (—): $\alpha = 0.981$, ($\cdots$): $\alpha = 1.03$. In the former case, the response reaches a periodic state in time, that corresponds to state III; in the latter, the response reaches the small-amplitude supercritical steady state.

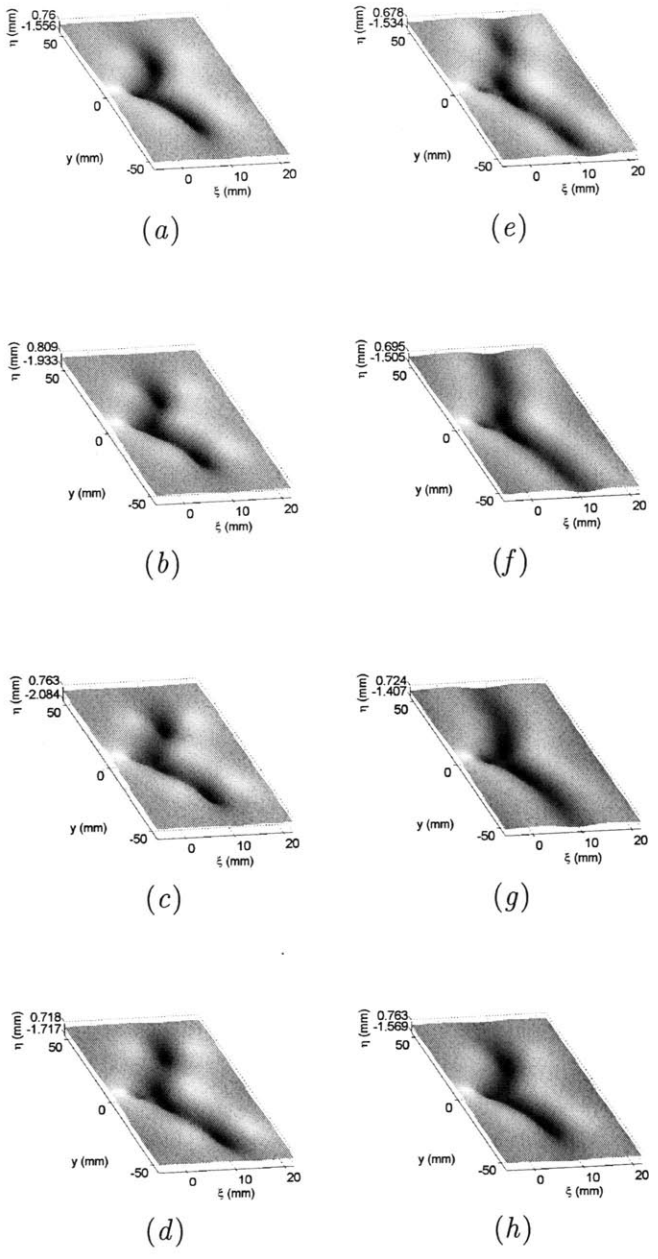

Figure 4-18: Plots at eight different time instants of the induced wave pattern for forcing amplitude $A = 0.23$, damping parameter $\tilde{\nu} = 2.4\tilde{\nu}_0$, where $\tilde{\nu}_0 = 0.003$, and forcing speed $\alpha = 0.981$. In (a), t=4.49 s and the following plots, (b)–(h), are separated by 0.36 s. The response corresponds to state III and is characterized by periodic shedding of lumps. The eight snapshots shown cover a full cycle of the shedding process, in qualitative agreement with the experimentally observed state III (figure 4-5).

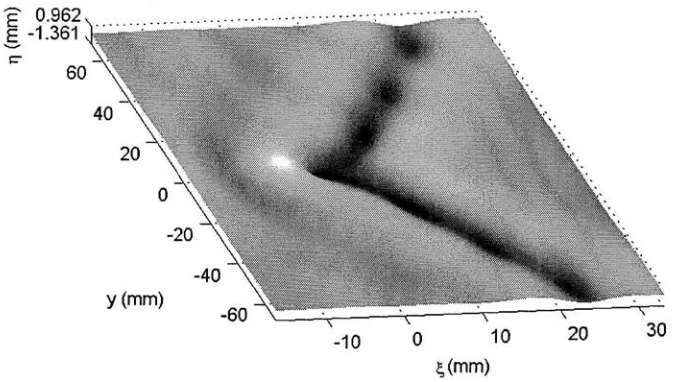

Figure 4-19: Plot of supercritical steady state reached by transient response from rest for forcing amplitude $A = 0.23$, damping parameter $\tilde{\nu} = 2.4\tilde{\nu}_0$, where $\tilde{\nu}_0 = 0.003$, and forcing speed $\alpha = 1.03$.

4.6 Discussion

The preceding analysis reveals that the precise nature of the forced response near the critical speed $c_{\min}$ is determined by a rather delicate balance between nonlinearity, which is controlled by the strength of forcing, and viscous dissipation. Out of the three possible subcritical responses found, state II and III, being nonlinear, are particularly sensitive to this interplay of nonlinear and damping effects. As a result, damping has to exceed a certain threshold in order for state II to be steady as observed experimentally rather than time-periodic, and state III ceases to be available when forcing is too weak in comparison to damping.

From a theoretical viewpoint, the prominent role that nonlinearity plays near $c_{\min}$ is perhaps somewhat surprising. It is easy to show (from either the model equation (4.8) or the full water-wave equations) that, ignoring dissipation, the linear response to localized forcing at speed equal to $c_{\min}$ features only a logarithmic singularity, and one might expect that damping would entirely mask nonlinear effects due to this weak resonance. Nevertheless, for forcing speed slightly below $c_{\min}$, the response exhibits rich nonlinear behaviour, which must be attributed to the presence of lumps in the

subcritical speed range.

In spite of being crude in many respects, the theoretical model proposed here reproduces, at least qualitatively, the main features of the observed responses, and seems to be a viable alternative to fully numerical simulation of the exact governing equations. This type of model could also prove useful in understanding the generation of gravity–capillary lumps in wind-wave experiments (Zhang 1995), as well as in other physical systems where the phase speed features a minimum at non-zero wavenumber (Squire *et al.* 1996).

Chapter 5

Concluding remarks

5.1 Summary and conclusion

The main purpose of the present thesis work is to reveal the physics governing the dynamic behavior of 3-D gravity–capillary depression solitary waves generated by a moving pressure forcing on the surface of deep water. Companion experiments were conducted by Dr. James Diorio and Professor James Duncan at University of Maryland. In the experiment, they made an observation of surface profiles according to forcing speeds. In summary, three different behavioral states (state I, II, and III) are identified according to forcing speeds. When the forcing speed is low, a simple 3-D depression was observed just below the moving forcing. This is essentially the linear response, and this state is refered to as state I. As the forcing speed is increased towards $c_{\min}$, they observed steep steady 3–D gravity-capillary solitary depression waves following just behind the moving forcing, and this state is referred to as state II. In addition, in state II, the response of maximum depression is independent of the forcing strength. Finally, near the resonance when forcing speed is close to $c_{\min}$, they observed that 3-D gravity-capillary solitary depression waves are shed outward in the oblique directions in a time-periodic manner and decay due to viscous dissipation. This state is referred to as state III. Overall, 3-D gravity–capillary solitary depression waves observed in the experiment are steep and, therefore, nonlinearity is not weak. In addition, they are in the gravity–capillary range, so viscous dissipation cannot be

neglected. Finally, the interplay between nonlinearity and viscous dissipation is very delicate, which is implied in the characteristics of state II and state III.

Chapter 2 deals with the stability and nonlinear dynamics of free 3-D gravity–capillary solitary depression waves. This chapter is related to the existence of stable steep 3-D gravity–capillary solitary depression waves observed in the companion experiment. A linear stability analysis reveals that 3-D gravity–capillary solitary depression waves are unstable in the small-amplitude limit, but become stable as the steepness increases. In other words, an exchange of stability occurs at a certain finite wave steepness. In addition, depending on the perturbation, the unstable small-amplitude 3-D gravity–capillary solitary depression wave either decays into dispersive waves or evolves into an oscillatory state near a stable steep 3-D gravity–capillary solitary depression waves. This chapter provides the theoretical proof for the existence of stable steep 3-D gravity–capillary solitary depression waves observed in the companion experiment.

Chapter 3 deals with the nonlinear dynamics of forced 2-D gravity–capillary solitary depression waves with viscous dissipation. This chapter is a preliminary study leading into the investigation of forced 3-D gravity–capillary solitary depression waves with viscous dissipation. Based on the unsteady simulation, three different behavioral states are identified according to the forcing speeds. When the forcing speed is low, a simple 2-D depression was calculated just below the moving forcing. This is essentially linear response. However, as the forcing speed is increased towards $c_{\min}$, a steady 2-D gravity–capillary solitary depression wave following just behind the moving forcing is identified. Finally, near the resonance when the forcing speed is close to $c_{\min}$, 2-D gravity–capillary solitary depression waves are shed outward in the streamwise direction in a time-periodic manner and decay due to viscous dissipation. This work provides a partial explanation for the three different behavioral states in the companion 3-D experiments.

Chapter 4 deals with the nonlinear dynamics of forced 3-D steep gravity–capillary solitary depression waves with viscous dissipation. A theoretical model equation is proposed accounting for the effects of three-dimensionality, unsteadiness, nonlinearity,

dispersion, dissipation and forcing; these physical effects are included in a straightforward manner and play important roles in providing a physical explanation for the dynamic behavior of 3-D gravity–capillary solitary depression waves in the experiments. Based on the unsteady simulation, three different behavioral states are identified according to forcing speeds. When the forcing speed is low, a simple 3-D depression was calculated just below the moving forcing. This is essentially the linear response and corresponds to state I in the companion experiment. However, as the forcing speed is increased towards $c_{\min}$, steady 3-D gravity–capillary solitary depression waves following just behind the moving forcing is identified. This state corresponds to state II in the companion experiment. Finally, near the resonance when the forcing speed is close to $c_{\min}$, 3-D gravity–capillary solitary depression waves are shed in the oblique directions in time-periodic manner and decay due to viscous dissipation. Based on the numerical continuation, the transitions from state I to II and from state II to III oberserved in the companion experiment turn out to be associated with certain limit points in the steady-state response diagram. In addition, in state II, the response of maximum depression is independent of the forcing strength, in agreement with the companion experiment.

5.2 Further studies and possible applications

The proposed model equation approach in the present thesis work is generic. This approach can be used in any wave system where the dispersion relation is known. Particularly, this approach will be useful in studying the wave system where the linear phase speed features a minimum at non-zero wavenumber. Physical examples are flexural–gravity waves on floating ice sheet (Hosking, Sneyd & Waugh 1988), envelope solitary waves on a thin shell (Wu *et al.* 1987), interfacial waves between two liquids (Kim & Akylas 2006).

There are possbile scientific and engineering applications related to the physics of 3-D gravity–capillary solitary waves revealed in the present thesis work.

The first example is the generation mechanism of ripples by wind (Zhang 1995).

The ripples can be modeled as 3-D gravity–capillary solitary depression waves, and wind can be modeled as multiple moving forcings which have both normal and tangential components to the water surface.

The second example is the study of the wave drag associated with the motion of a small body on a free surface (Burghelea & Steinberg 1996). In this case, the small body on a free surface acts as a forcing. This study may be useful in drag calculations which are essential in the engineering design of small biomimetic robots or small unmanned vehicles on the water surface.

The third example is the possible application in micro-scale or nano-scale patterning using moving probes such as an Atomic Force Microscope (Raphaël & de Gennes 1996). In this case, for the clean and stable patterning and, also for the fast production, the physical results revealed from the present thesis work may provide the optimal working criteria (for example, optimal rigidity of materials, optimal speed range of moving probes).

The final example is the study of the wave drag assocated with the motion of ocean vehicles on the surface of ice-covered ocean in the arctic area (Takizawa 1988). People continue to explore this area for the possible natural resources and for water sources. In this arctic area, frequent fuel supply to the ocean vehicle is often very difficult. This study may be useful in drag calculations which may be helpful in the design of low fuel-consumption ocean vehicles operating on the ice-covered surface.

Appendix A

Spectral method: steady, free, inviscid model equation

Spectral method is used to solve the following steady, free, inviscid equation.

$$(\alpha - \tfrac{1}{2})\eta_\xi - (\beta\eta^2)_\xi - \tfrac{1}{4}\mathcal{H}\{\eta_{\xi\xi} + 2\eta_{yy} - \eta\} = 0 \tag{A.1}$$

Rather than solving the above partial differential equation in the real domain (ξ,y), we can solve it in the wavenumber (spatial frequency) domain (k,l). In other words, using spatial Fourier Transform, we transform the partial differential equation (A.1) into the following algebraic equation in the wavenumber domain.

$$[(\alpha - \tfrac{1}{2})\mathrm{i}k - \tfrac{1}{4}\mathrm{isgn}(k)(k^2 + 2l^2 + 1)]\hat{\eta} = \beta\mathrm{i}k\hat{\eta^2} \tag{A.2}$$

where, $\hat{\eta}(k,l) = FT\{\eta(\xi,y)\}$. The above algebraic equation (A.2) is solved numerically in the wavenumber domain. The solution found in the wavenumber domain is then transformed into the solution in the real domain using Inverse Fourier Transform.

Appendix B

Quadratic and cubic nonlinearities

In the derivation of the model equation, rather than using only quadratic nonlinearity, we can adopt both quadratic and cubic nonlinearities with coefficients β_1 and β_2 respectively, as follows.

$$\eta_t + (\alpha - \tfrac{1}{2})\eta_\xi - (\beta_1\eta^2 + \beta_2\eta^3)_\xi - \tfrac{1}{4}\mathcal{H}\left\{\eta_{\xi\xi} + 2\eta_{yy} - \eta\right\} = 0 \tag{B.1}$$

In the small-amplitude limit near $\alpha = 1$, the solution of (B.1) can be expanded as

$$\eta = \tfrac{1}{2}\epsilon\left\{S(X,Y)\mathrm{e}^{\mathrm{i}\xi} + \text{c.c.}\right\} + \tfrac{1}{2}\epsilon^2\left\{S_2(X,Y)\mathrm{e}^{2\mathrm{i}\xi} + \text{c.c.}\right\} + \cdots, \tag{B.2}$$

As a result, the associated nonlinear Schrödinger equation for S is governed by

$$-S + \tfrac{1}{4}(S_{XX} + 2S_{YY}) + \tfrac{1}{4}(16\beta_1^2 - 3\beta_2)S^2S^* = 0. \tag{B.3}$$

In addition, the relation between S and S_2 is

$$S_2 = -4\beta_1 S^2. \tag{B.4}$$

On the other hand, if the expansion (B.2) is used in the full water wave equations, we find the following two equations which correspond to (B.3) and (B.4) respectively.

$$-S + \tfrac{1}{4}(S_{XX} + 2S_{YY}) + \tfrac{11}{32}S^2S^* = 0. \tag{B.5}$$

$$S_2 = -S^2. \tag{B.6}$$

From (B.3)–(B.6), by comparison, the coefficients of quadratic and cubic nonlinearities are found to be $\beta_1 = 1/4$ and $\beta_2 = -1/8$.

Appendix C

Pseduo-arclength continuation method: steady, forced, inviscid/viscous model equation

Pseudo-arclength continuation method is used to solve the following steady, forced, inviscid/viscous equation.

$$-\tilde{\nu}(\eta_{\xi\xi} + \eta_{yy}) + (\alpha - \tfrac{1}{2})\eta_{\xi} - \beta(\eta^2)_{\xi} - \tfrac{1}{4}\mathcal{H}\{\eta_{\xi\xi} + 2\eta_{yy} - \eta\} = Ap_{\xi} \qquad \text{(C.1)}$$

where, $\tilde{\nu} \geq 0$. Since the above equation (C.1) is a nonlinear partial differential equation, multiple solutions can exist for a certain value of α in the abstract (α, η) space. To find out multiple solutions $\eta(\xi, y)$, instead of treating α as a fixed parameter, we treat α as another solution in the given equation (C.1) as follows.

$$G(\eta, \alpha) = -\tilde{\nu}(\eta_{\xi\xi} + \eta_{yy}) + (\alpha - \tfrac{1}{2})\eta_{\xi} - \beta(\eta^2)_{\xi} - \tfrac{1}{4}\mathcal{H}\{\eta_{\xi\xi} + 2\eta_{yy} - \eta\} - Ap_{\xi} = 0 \quad \text{(C.2)}$$

Therefore, to find the solution set (α, η), another equation, which is related to pseudo-arclength, is introduced.

$$F(\eta, \alpha) = s(\eta - \eta_0) + \sigma(\alpha - \alpha_0) - \Delta S = 0 \qquad \text{(C.3)}$$

Here, (α_0, η_0) is a previous solution set, (α, η) is the adjacent solution set to be found on the solution branch, $\hat{t} = (\sigma, s)$ is a unit-length tangent or a unit-length pseudo-arch at (α_0, η_0) on the solution branch, and ΔS is the pseudo-arclength which can be controlled. The simultaneous equation system (C.2) and (C.3) for (α, η) can be solved numerically. The newly found solution set (α, η) plays a role as (α_0, η_0) in finding out the next solution set on the solution branch, and this procedure can be continued.

Appendix D

Spectral method in space and predictor-corrector method in time: unsteady, forced, viscous model equation

Spectral method in space and predictor-corrector method (Semi-implict Euler or Improved Euler) in time are used to solve the following unsteady, forced, viscous equation.

$$\eta_t - \tilde{\nu}(\eta_{\xi\xi} + \eta_{yy}) + (\alpha - \tfrac{1}{2})\eta_\xi - \beta(\eta^2)_\xi - \tfrac{1}{4}\mathcal{H}\{\eta_{\xi\xi} + 2\eta_{yy} - \eta\} = Ap_\xi \qquad \text{(D.1)}$$

Rather than solving the above partial differential equation in the real domain (ξ,y), we can solve it in the wavenumber (spatial frequency) domain (k,l). In other words, using spatial Fourier Transform, we transform the partial differential equation (D.1) into the following ordinary differential equation in the wavenumber domain.

$$\hat{\eta}_t = -[\tilde{\nu}(k^2 + l^2) + (\alpha - \tfrac{1}{2})\mathrm{i}k - \tfrac{1}{4}\mathrm{isgn}(k)(k^2 + 2l^2 + 1)]\hat{\eta} + \beta\mathrm{i}k\hat{\eta^2} + \mathrm{i}kA\hat{p} \qquad \text{(D.2)}$$

where, $\hat{\eta}(k,l,t) = FT\{\eta(\xi,y,t)\}$ and $\hat{p}(k,l) = FT\{p(\xi,y)\}$. Now, the predictor-corrector method is used to solve the above ordinary differential equation (D.2) in the wavenumber domain. For simplicity, we can denote the right hand side of (D.2) as $F(\hat{\eta})$.

$$\hat{\eta}_t = F(\hat{\eta}) \tag{D.3}$$

The predictor-corrector method is composed of two steps. The first step is the prediction step.

$$\hat{\eta}_p^{n+1} = \hat{\eta}^n + \Delta t F(\hat{\eta}^n) \tag{D.4}$$

where, Δt is the numerical time step, $\hat{\eta}_p^{n+1}$ denotes the predicted $\hat{\eta}(k,l,(n+1)\Delta t)$ and $\hat{\eta}^n$ denotes the $\hat{\eta}(k,l,n\Delta t)$. The second step is the correction step.

$$\hat{\eta}^{n+1} = \hat{\eta}^n + \frac{\Delta t}{2}\left\{F(\hat{\eta}_p^{n+1}) + F(\hat{\eta}^n)\right\} \tag{D.5}$$

where, $\hat{\eta}^{n+1}$ denotes the $\hat{\eta}(k,l,(n+1)\Delta t)$. The solution found in the wavenumber domain, then, will be transformed into the solution in the real domain using spatial Inverse Fourier Transform.

Bibliography

[1] M. Ablowitz, I. Bakirtas, and B. Ilan. Wave collapse in a class of nonlocal nonlinear Schrödinger equations. *Physica D*, 207:230–253, 2005.

[2] M. J. Ablowitz and H. Segur. On the evolution of packets of water-waves. *Journal of Fluid Mechanics*, 92:691–715, 1979.

[3] B. Akers and P. A. Milewski. A model equation for wavepacket solitary waves arising from capillary–gravity flows. *Studies in Applied Mathematics*, 122:249–274, 2009.

[4] T. R. Akylas. On the excitation of long nonlinear water-waves by a moving pressure distribution. *Journal of Fluid Mechanics*, 141:455–466, 1984.

[5] T. R. Akylas. On the excitation of nonlinear water-waves by a moving pressure distribution oscillating at resonant frequency. *Physics of Fluids*, 27:2803–2807, 1984.

[6] T. R. Akylas. Envelope solitons with stationary crests. *Physics of Fluids A*, 5:789–791, 1993.

[7] T. R. Akylas. Three-dimensional long water-wave phenomena. *Annual Review of Fluid Mechanics*, 26:191–210, 1994.

[8] T. R. Akylas and Y. Cho. On the stability of lumps and wave collapse in water waves. *Philosophical Transactions of the Royal Society A*, 366:2761–2774, 2008.

[9] D. J. Benney and G. J. Roskes. Wave instabilities. *Studies in Applied Mathematics*, 48:377–385, 1969.

[10] T. Burghelea and V. Steinberg. Wave drag due to generation of capillary–gravity surface waves. *Physical Review E*, 66:051204.1–051204.13, 1996.

[11] D. C. Calvo and T. R. Akylas. Stability of steep gravity–capillary solitary waves in deep water. *Journal of Fluid Mechanics*, 452:123–143, 2002.

[12] D. C. Calvo, T.-S. Yang, and T. R. Akylas. On the stability of solitary waves with decaying oscillatory tails. *Proceedings of the Royal Society A*, 456:469–487, 2000.

[13] Y. Cho and T. R. Akylas. Forced waves near resonance at a phase-speed minimum. *Studies in Applied Mathematics*, 123:1–15, 2009.

[14] S. L. Cole. Transient waves produced by flow past a bump. *Wave Motion*, 7:579–587, 1985.

[15] A. Davey and K. Stewartson. Three-dimensional packets of surface-waves. *Proceedings of the Royal Society A*, 338:101–110, 1974.

[16] F. Dias and C. Kharif. Nonlinear gravity and capillary–gravity waves. *Annual Review of Fluid Mechanics*, 31:301–346, 1999.

[17] J. Diorio, Y. Cho, J. H. Duncan, and T. R. Akylas. Gravity–capillary lumps generated by a moving pressure source. *Physical Review Letters*, 103:214502, 2009.

[18] V. D. Djordjevic and L. G. Redekopp. On two-dimensional packets of capillary–gravity waves. *Journal of Fluid Mechanics*, 79:703–714, 1977.

[19] R. Grimshaw and B Malomed. New type of gap soliton in a coupled Korteweg–de Vries wave system. *Physical Review Letters*, 72:949–953, 1994.

[20] R. H. J. Grimshaw, editor. *Solitary Waves in Fluids.* WIT Press, Southhampton, UK, 2007.

[21] R. H. J. Grimshaw and N. Smyth. Resonant flow of a stratified fluid over topography. *Journal of Fluid Mechanics*, 169:429–464, 1986.

[22] M. D. Groves and S. M. Sun. Fully localised solitary-wave solutions of the three-dimensional gravity–capillary water-wave problem. *Archive for Rational Mechanics and Analysis*, 188:1–91, 2008.

[23] R. J. Hosking, A. D. Sneyd, and D. W. Waugh. Viscoelastic response of a floating ice plate to a steadily moving load. *Journal of Fluid Mechanics*, 196:409–430, 1988.

[24] B. B. Kadomtsev and V. I. Petviashvili. On the stability of solitary waves in weakly dispersive media. *Soviet Physics-Doklady*, 15:539–541, 1970.

[25] S. C. Kak. Discrete Hilbert transform. *Proceedings of the Institute of Electrical and Electronics Engineers*, 58:585–586, 1970.

[26] Y. Kang and J. M. Vanden-Broeck. Gravity–capillary waves generated by a moving pressure distribution in the presence of constant vorticity and dissipation. *Computers and Fluids*, 34:876–890, 2005.

[27] C. Katsis and T. R. Akylas. On the excitation of long nonlinear water-waves by a moving pressure distribution. Part 2: Three-dimensional effects. *Journal of Fluid Mechanics*, 177:49–65, 1987.

[28] B. Kim and T. R. Akylas. On gravity-capillary lumps. *Journal of Fluid Mechanics*, 540:337–351, 2005.

[29] B. Kim and T. R. Akylas. On gravity-capillary lumps. Part 2. Two-dimensional Benjamin equation. *Journal of Fluid Mechanics*, 557:237–256, 2006.

[30] B. Kim and T. R. Akylas. Transverse instability of gravity-capillary solitary waves. *Journal of Engineering Mathematics*, 58:167–175, 2007.

[31] D. Korteweg and G. de Vries. On the change of form of long waves advancing in a rectangular channel and a new type of long stationary waves. *Philosophical Magazine*, 38:422–443, 1895.

[32] H. Lamb. *Hydrodynamics.* Cambridge University Press, West Nyack, NY, 1993.

[33] M. Longuet-Higgins and X. Zhang. Experiments on capillary-gravity waves of solitary type on deep water. *Physics of Fluids*, 9:1963–1968, 1997.

[34] M. S. Longuet-Higgins. Capillary–gravity waves of solitary type on deep water. *Journal of Fluid Mechanics*, 200:451–470, 1989.

[35] M. S. Longuet-Higgins. Capillary gravity–waves of solitary type and envelope solitons on deep-water. *Journal of Fluid Mechanics*, 252:703–711, 1993.

[36] M. S. Longuet-Higgins. Viscous dissipation in steep capillary–gravity waves. *Journal of Fluid Mechanics*, 344:271–289, 1997.

[37] Z. H. Musslimani and J. Yang. Self-trapping of light in a two-dimensional photonic lattice. *Journal of the Optical Society of America B*, 21:973–981, 2004.

[38] G. C. Papanicolaou, C. Sulem, P. L. Sulem, and X. P. Wang. The focusing singularity of the Davey-Stewartson equations for gravity–capillary surface-waves. *Physica D*, 72:61–86, 1994.

[39] E. Parau and F. Dias. Nonlinear effects in the response of a floating ice plate to a moving load. *Journal of Fluid Mechanics*, 460:281–305, 2002.

[40] E. Parau, J.-M. Vanden-Broeck, and M. J. Cooker. Three-dimensional capillary–gravity waves generated by a moving disturbance. *Physics of Fluids*, 19:082102–082107, 2007.

[41] E. I. Parau, J. M. Vanden-Broeck, and M. J. Cooker. Nonlinear three-dimensional gravity–capillary solitary waves. *Journal of Fluid Mechanics*, 536:99–105, 2005.

[42] L. Paumond. Towards a rigorous derivation of the fifth order KP equation. *Mathematics and Computers in Simulation*, 69:477–491, 2005.

[43] D. Pelinovsky and R. H. J. Grimshaw. Asymptotic methods in soliton stability theory. In L. Debnath and S. R. Choudhury, editors, *Nonlinear instability analysis Advances in fluid mechanics*, volume 12, pages 245–312. Computational Mechanics Publications, Southampton, UK and Billerica, MA, 1997.

[44] E. Raphaël and P. G. deGennes. Capillary gravity waves caused by a moving disturbance: Wave resistance. *Physical Review E*, 53:3448–3455, 1996.

[45] D. Richard and E. Raphaël. Capillary–gravity waves: The effect of viscosity on the wave resistance. *Europhysics Letters*, 48:49–52, 1999.

[46] S. Russell. Report on waves. *Report of the fourteenth meeting of the British Association for the Advancement of Science, York*, pages 311–390, 1844.

[47] V. A. Squire, R. J. Hosking, A. D. Kerr, and P. J. Langhorne. *Moving Loads on Ice Plates.* Kluwer Academic Publishers, Norwell, MA, 1996.

[48] V. A. Squire, W. H. Robinson, P. J. Langhorne, and T. G. Haskell. Vehicles and aircraft on floating ice. *Nature*, 333:159–161, 1988.

[49] J. T. Stuart. On the non-linear mechanics of wave disturbances in stable and unstable parallel flows. Part 1. The basic behaviour in plane Poiseuille flow. *Journal of Fluid Mechanics*, 9:353–370, 1960.

[50] T. Takizawa. Response of a floating sea ice-sheet to a steadily moving load. *Journal of Geophysical Research*, 93:5100–5112, 1988.

[51] J. M. Vanden-Broeck and F. Dias. Gravity–capillary solitary waves in water of infinite depth and related free-surface flows. *Journal of Fluid Mechanics*, 240:549–557, 1992.

[52] G. B. Whitham. *Linear and Nonlinear Waves.* Wiley-Interscience, New York, NY, 1974.

[53] J. Wu, J. Weatly, S. Putterman, and I. Rudnick. Observation of envelope solitons in solids. *Physical Review Letters*, 59:2744–2747, 1987.

[54] T. Y. Wu. Generation of upstream advancing solitons by moving disturbances. *Journal of Fluid Mechanics*, 184:75–99, 1987.

[55] T.-S. Yang and T. R. Akylas. On asymmetric gravity-capillary solitary waves. *Journal of Fluid Mechanics*, 330:215–232, 1997.

[56] X. Zhang. Capillary–gravity and capillary waves generated in a wind-wave tank: Observations and theories. *Journal of Fluid Mechanics*, 289:51–82, 1995.